Journal of Alloys and Compounds 898 (2022) 162865

Contents lists available at ScienceDirect

Journal of Alloys and Compounds

journal homepage: www.elsevier.com/locate/jalcom

An experimental and theoretical investigation on structure-property correlation of $Cu_2Mn_1Al_{1-x}Ga_x$ full-Heusler alloy

Shashank Shekhar Mishra[a,b,*], Anurag Bajpai[a], Thakur Prasad Yadav[b,**], Ram Manohar Yadav[c,d,***], Anand B. Puthirath[d], Liangzi Deng[e], Moein Adnani[e], Ching-Wu Chu[e,f], Robert Vajtai[d], Pulickel M. Ajayan[d,**], Krishanu Biswas[a], Nilay Krishna Mukhopadhyay[g]

[a] Department of Materials Science and Engineering, Indian Institute of Technology Kanpur, Kanpur 208016, India
[b] Hydrogen Energy Centre, Department of Physics, Institute of Science, Banaras Hindu University, Varanasi 221005, India
[c] Department of Physics, VSSD College, Kanpur 208002, India
[d] Department of Materials Science and Nano Engineering, Rice University, Houston, USA
[e] Texas Center for Superconductivity and Department of Physics, University of Houston, Houston, TX, USA
[f] Lawrence Berkeley National Laboratory, Berkeley, CA 94720, USA
[g] Department of Metallurgical Engineering, Indian Institute of Technology (Banaras Hindu University), Varanasi 221005, India

ARTICLE INFO

Article history:
Received 2 July 2021
Received in revised form 7 November 2021
Accepted 17 November 2021
Available online 25 November 2021

Keywords:
Monovalent state
$L2_1$ structure
Interphase exchange coupling
Magnetic phase transition
Arrott plot
Gaussian process regression

ABSTRACT

The present study reports the evolution of microstructure and magnetic properties of $Cu_2MnAl_{1-x}Ga_x$ Heusler alloys. The $L2_1$ phase, which remained stable up to a Ga substitution of x = 0.3, transformed into mixed phases, i.e., hexagonal close packed (HCP) and complex cubic structure (CCS) on further addition of Ga. The non-monotonic increase in the lattice constant indicates that some amount of Ga retains its monovalent state. The magnetic phase showed a transition from ferromagnetic to paramagnetic state with increasing Ga concentration. The re-entrant temperature (T_R) decreased from 8.2 K to 5.2 K as Ga content increased from 5 at% to 10 at%. The strength of magnetic exchange-coupling also reduced with an increase in Ga content. Gaussian process regression (GPR) was used to estimate the lattice parameter using the ionic radii and Pauling electronegativity of the constituents. The modeling approach showed high accuracy and stability, providing new insights into future alloy development.

1. Introduction

The Heusler alloys have been extensively investigated during the last few decades and have become potential candidates for several applications such as shape memory materials, spin injection or spin electronics, and half-metallicity [1–7]. The stoichiometric composition of full Heusler alloy is X_2YZ, where X is a transition metal (i.e., X = Co, Cu, Fe, Ni, Pd. etc.), Y is manganese, and Z corresponds to a *sp* group element (i.e., Z = Al, Ga, Ge, Sn, In, etc.). The preferred site of the transition metal atoms (X, Y) is governed by their valence electrons and in accordance with the Pearson table [8], this alloy crystallizes into the $L2_1$ crystal structure. However, when the chemical disordering occurs, the structure may transform into B2-type. Some of the Heusler alloys exhibiting large perpendicular magnetic anisotropy crystallize into the tetragonal structure owning the potential for permanent-magnet applications and spin-transport torque (STT)-based memory [2,9]. Heusler alloys are also found to be very attractive for spintronics applications because they possess unique band structures of half-metals that are semiconducting or insulating for one spin channel and metallic for the opposite spin channel [10,11]. Therefore, theoretically, Heusler alloys can provide 100% spin polarization at room temperature [3,12–14]. According to several theoretical and experimental observations, it has been found that the inclusion of a tunnel barrier can improve spin injection efficiency [15,16]. But practically, it is not possible to fabricate tunnel barriers with high quality and long life. This issue can be solved by the application of highly spin-polarized ferromagnetic materials

* Corresponding author at: Department of Materials Science and Engineering, Indian Institute of Technology Kanpur, Kanpur 208016, India.
** Corresponding authors.
*** Corresponding author at: Department of Physics, VSSD College, Kanpur 208002, India.
E-mail addresses: smishra747@gmail.com (S.S. Mishra), yadavtp@gmail.com (T.P. Yadav), rmanohar28@gmail.com (R.M. Yadav), ajayan@rice.edu (P.M. Ajayan).

https://doi.org/10.1016/j.jallcom.2021.162865
0925-8388/

using Heusler alloys [17,18]. Generally, the Heusler alloys possess a high Curie temperature (T_C), and their lattice constants have a minute mismatch with most common semiconductors (GaAs, MgO). Hence, they are considered the most efficient materials for spintronics device electrodes [19].

The copper series Heusler alloys, particularly Cu_2MnAl alloys, were the most studied materials [20] because they show ferromagnetic behavior though their constituents are non-ferromagnetic [21]. The Cu_2MnAl Heusler alloys were already synthesized by several methods, such as pulsed laser deposition in bulk form, thin films via RF sputtering [21–23], etc. Most of the as-produced Heusler alloys need annealing treatment to transform into the ferromagnetic phase ($L2_1$ phase). The interface, bulk, and surface properties of Cu_2MnAl-type [24] as well as Hg_2CuTi-type Heusler compounds [25] have been extensively investigated and have been demonstrated greater application prospects in ultrahigh-speed reading in magnetic read heads of hard disk drivers (HDD), magnetic random access memory (MRAM) and spin-transfer torque (STT) devices [26–28]. The elemental substitution/doping has been vindicated as an effective way of strengthening the half-metallicity and adjusting the Fermi level in Heusler alloys [29]. A few investigations have also been conducted on the off-stoichiometric and stoichiometric Cu-Mn-Al Heusler alloy ribbons [30–37]. The addition of Ti and Ni in the off-stoichiometric Cu-Al-Mn system decreases the entropy, enthalpy, and hysteresis values and changes the austenite to martensite transformation temperature [31]. The Cu-Mn-Al-V alloy exhibits excellent superelastic characteristics [32]. The partial replacement of Al by Ga in Cu-Mn-Al ribbons gives rise to the evolution γ-Cu_9Al_4 (i.e., simple cubic gamma brass type) phase co-existing with the parent $L2_1$ phase and decreases the saturation magnetization [33]. When Al was replaced by Sn in the Cu-Mn-Al system, it showed ideal resistivity, varying with T^5 at low temperatures. This behavior is unusual for ferromagnetic materials, and it was further observed that above T_C, it was structurally unstable [34]. Recently, the authors have investigated the effect of Ga substitution on the structural and magnetic properties of Fe-Mn-Al Heusler alloy and observed that the Curie temperature decreases with the progressive increase in Ga atomic fraction. In contrast, lattice expands linearly with an increase in Ga content [38].

Block et al. [39] have reported that in half and full Heusler alloys, the half-metallic character is affected by a small variation in the lattice parameters, influencing the magnetic nature. Ishikawa et al. [40] have observed that Ga substitution in $Ni_2MnGa_xAl_{1-x}$ alloy stabilizes the $L2_1$ structure and remarkably affects the magnetic response. Hence, examining how the structural and magnetic properties are governed by the lattice parameter variation attributed to the elemental substitution will be interesting. The desired structural, magnetic, and electronic properties can be achieved by replacing or adding a suitable element at a particular lattice site [21,32,34]. Ga is similar to Al in terms of valance electrons and oxidation state (rarely Ga^{1+}), but it differs in size and surface energy. Al possesses surface energy twice that of Ga [41]. It has been observed that when Ga attains the monovalent state, the Fermi level, Fermi energy and e/a ratio vary, and it influences the tribological behavior [42,43]. Hence, it will be worthwhile to investigate how Al substitution by Ga affects the properties in Cu_2MnAl(Ga) Heusler alloys.

In the present work, the authors have investigated the structural and magnetic properties of $Cu_2Mn_1Al_{1-x}Ga_x$ (x = 0, 0.10, 0.20, 0.25, 0.28, 0.30, 0.40) Heusler alloys synthesized by induction melting. To get a series with the general formula of $Cu_2Mn_1Al_{1-x}Ga_x$ ($0 \le x \le 0.40$), we have chosen Ga as a doping element at the Al site, starting with the parent stoichiometric composition Cu_2MnAl. Further, band structure calculations have revealed that a small amount of disorder in the atomic distribution on the lattice sites can cause significant changes in the electronic structure and magnetic properties of Heusler alloys. The lattice constant, estimated through experiments, is used in various studies for band structure calculations. The dependence on the experimental estimation of lattice constant limits the exploration of new Heusler compounds that have not been synthesized. To overcome this obstacle, linear regression and neural network models have recently been used to estimate and predict cubic perovskites lattice constants, providing alternative approaches to predicting lattice constants with limited information [44]. With this background, a Gaussian process regression (GPR) model has also been designed in the present study to estimate the lattice parameter a_o of Heusler alloys using its mathematical relationship with the ionic radii of the alloying elements and the Pauling electronegativity of element Z. The GPR model has previously been used in the case of other alloy systems and materials as an intelligent computational technique to predict critical physical parameters for various applications [45–47]. The designed model can aid in designing new Heusler compounds with desired lattice constants for further research into their electronic structures and functional applications.

2. Materials and methods

2.1. Alloy synthesis

The polycrystalline ingots with nominal composition $Cu_2MnAl_{1-x}Ga_x$ (x = 0, 0.10, 0.20, 0.25, 0.28, 0.30, 0.40) were fabricated utilizing 18 kW induction furnace. The melting was performed with high purity constituent elements (i.e., Fe, Mn, Al, Ga) in a dynamic argon atmosphere to prevent oxide formation during melting. The constituents were taken in an appropriate proportion and pelletized into a circular button of 15 mm diameter for the desired composition by applying hydraulic pressure. This button was placed inside a quartz tube surrounded by a Pyrex glass jacket, maintaining a continuous cold-water flow through it. The uninterrupted flow of argon created an inert atmosphere. To ensure chemical homogenization, the ingot buttons were flipped over and re-melted several times.

2.2. Characterization

The gross structure of the samples was analyzed by the X-ray diffraction (XRD) technique using the PANalytical Empyrean instrument with CuK_α (λ = 1.5406 Å) radiation. The XRD data was recorded in continuous scan mode at a working voltage of 45 kV and current 30 mA and a scan rate of 0.013°in the 2θ range of 10–100°. All the experimental parameters and conditions, such as scan speed, step size, etc., were kept identical for all the samples. The surface morphology was examined by optical microscope (Olympus BX51M) and scanning electron microscopy (QUANTA 200) operated at 25 kV. The samples were etched before optical microanalysis using $FeCl_3$ (1 gm) + 5 ml HCl + 12 ml ethanol solution. The chemical composition was analyzed using an energy dispersive X-ray spectrometer (EDS) coupled with a scanning electron microscope. The compositional homogeneity was ascertained using wavelength dispersive spectroscopy (WDS) through Electron probe microanalyzer (EPMA) (Jeol, JXA-8230). The Tecnai $20G^2$ operating at 200 kV electron microscope (TEM) was utilized to explore the microstructural features in more detail. The local area compositional analysis was also done to ensure the purity and homogeneity of the alloys. The DC magnetization measurements were carried out using Magnetic Property Measurement System (MPMS) by Quantum Design at the temperature down to 2 K and magnetic field up to 5 T.

2.3. Modelling methodology

MATLAB has been used in the present study for performing computations and simulations. The experimental dataset of reported Heusler alloys has been constructed using the available literature and summarized in Supporting Information, Table ST1. The dataset is made with attention towards selecting a broad range of Heusler compounds encompassing metals, half-metals, and semiconductors. A total of 308 Heusler alloys (X_2YZ) with a_o ranging from 3.95 Å to 6.95 Å (Supporting Information, Table ST1) have been selected for the present study. Z is mainly chosen from Al, Si, Sn, Ge, Ga, In, Sb, P, and As to expand the compositional space and variety. The predictor space chosen for the current regression study consists of ionic radii of X, Y, and Z, as well as the Pauling electronegativity of Z. The values for these parameters, have been summarized in Supporting Information, Table ST1. The model used to perform a regression analysis in the present study is the Gaussian Process Regression model [48,49], a non-parametric kernel-based probabilistic model. The dataset has been classified randomly into the training set consisting of 262 (~85%) alloys and the testing set containing the remaining 46 Heusler alloys.

The present study uses four kernel functions within the GPR algorithm, namely Exponential, Squared Exponential, Rational Quadratic, and Matern 5/2 [48,49], explained using Eqs. (1)–(4), respectively.

$$k(x_i, x_j|\beta) = \sigma_f^2 exp\left(-\frac{r}{\sigma_l}\right) \tag{1}$$

$$k(x_i, x_j|\beta) = \sigma_f^2 \exp\left[-\frac{1}{2}\frac{(x_i - x_j)^T(x_i - x_j)}{\sigma_l^2}\right] \tag{2}$$

$$k(x_i, x_j|\beta) = \sigma_f^2\left(1 + \frac{\sqrt{5}r}{\sigma_l} + \frac{5r^2}{3\sigma_l^2}\right)exp\left(-\frac{\sqrt{5}r}{\sigma_l}\right) \tag{3}$$

$$k(x_i, x_j|\beta) = \sigma_f^2\left(1 + \frac{r^2}{2\alpha\sigma_l^2}\right)^{-\alpha} \tag{4}$$

where σ_l is the length scale describing the distance between two variables to be considered uncorrelated, σ_f is the signal standard deviation, $r = \sqrt{(x_i - x_j)^T(x_i - x_j)}$ and α is a positive-valued scale-mixture parameter. The values of σ_f and σ_l must be positive and can be interpreted using β as $\beta_1 = \log \sigma_l$ and $\beta_2 = \log \sigma_f$.

The performance of the GPR model has been evaluated using the correlation coefficient (CC), mean absolute error (MAE), and root mean square error (RMSE). These criteria have been calculated using Eqs. (5)–(7), respectively.

$$CC = \frac{\sum_{i=1}^{n}(x_i^{exp} - \bar{x}^{exp})(x_i^{pre} - \bar{x}^{pre})}{\sqrt{\sum_{i=1}^{n}(x_i^{exp} - \bar{x}^{exp})^2 \sum_{i=1}^{n}(x_i^{pre} - \bar{x}^{pre})^2}} \tag{5}$$

$$\text{MAE} = \frac{1}{n}\sum_{i=1}^{n}|x_i^{exp} - x_i^{pre}| \tag{6}$$

$$\text{RMSE} = \sqrt{\frac{1}{n}\sum_{i=1}^{n}(x_i^{exp} - x_i^{pre})^2} \tag{7}$$

where, n is the size of the dataset. x_i^{exp} and x_i^{pre} are experimental and predicted values of a_o (Å) for the i^{th} composition, and $\bar{x}^{exp}$ and $\bar{x}^{pre}$ are their average values.

3. Results and discussion

3.1. Structural observations

The effect of Ga on the phase stability of $Cu_2MnAl_{1-x}Ga_x$ Heusler alloy before and after partial substitution of Al by Ga at different concentrations was investigated. Supporting Information, Fig. S1 shows the XRD pattern of $Cu_2MnAl_{1-x}Ga_x$ (x = 0, 0.28, 0.40) Heusler alloys measured at room temperature. In Heusler alloys, different types of atomic ordering may be observed. When all the Cu, Mn and Al atoms reside at their respective lattice sites, it crystallizes into a completely ordered state characterized by $L2_1$ structure. A B2-type ordering comes into play if Mn and Al randomly occupy their sites while Cu atoms are found at the proper site in the body-centered cubic (BCC) lattice. If the lattice site was randomly occupied by all constituents (Cu, Mn, and Al), it produces a simple BCC structure called A2-type. The parent Cu_2MnAl(x = 0) alloy crystallizes into ordered $L2_1$ structure (a = 5.9749 Å, space group Fm-3 m) consisting of four interpenetrating face-centered cubic (FCC) lattices (Supporting Information, Fig. S1(a)). It preserves the parent crystal structure ($L2_1$ phase) up to x = 0.28 alloy (Supporting Information, Fig. S1(b)). However, the peak intensity, peak position and peak broadening were affected by Ga content. The effect of Ga substitution in this phase ($L2_1$) will be discussed later. It is remarkable to note that as the Ga content increases from x = 0.28 to x = 0.30, a sharp structural transformation occurs in Supporting Information, Fig. S1(c). The alloy of x = 0.30 exhibits a biphasic nature. These new phases have been successfully indexed with hexagonal closed pack (HCP) structure (Cu_3Mn_2Ga-type, space group $P6_3/mmc$) with lattice parameter a = 4.9207 Å and c = 7.9484 Å and complex cubic structure (Cu_9Al_4-ordered gamma brass type, space group P-43 m) with lattice parameter a = 8.7232 Å.

In order to determine the effect of Ga substitution on the crystal structure of $Cu_2MnAl_{1-x}Ga_x$ (x = 0, 0.10, 0.20, 0.25, 0.28) alloys, the XRD measurement has been performed on these alloys and given in Supporting Information, Fig. S2. The simulated XRD pattern of the parent composition, i.e., Cu_2MnAl alloy (a = 5.949 Å, space group Fm-3 m) for the ordered $L2_1$ Heusler structure, has been given in Supporting Information, Fig. S2(a) for the sake of comparison with the experimental XRD patterns. In the experimental XRD patterns, some of the diffraction peaks such as (311), (222) and (331) were absent, and relative intensity was not in proportion because of the texturing of the polycrystalline sample (Supporting Information, Fig. S2(b–f)). For the full Heusler (X_2YZ) compounds, the (111) lattice plane reflects the chemical ordering of Y and Z atoms, while the (200) reflection is indicative of the superlattice reflections arising from X atoms. The (220), (400), (420) and (440) reflection was considered as body-centered cubic (BCC) fundamental lattice reflections [50]. The presence of (111) reflection shows the ordered occupation of Al/Ga and Mn atoms at the lattice sites. The intensity of (111) reflection decreases as the Ga content increases, indicating an enhancement in the site occupation disordering of Mn and Al/Ga atoms for higher Ga content alloys (Supporting Information, Fig. S2(b–f)). The ordering in the Cu sublattice was confirmed by (200) superlattice diffraction peak and was found consistent for all other alloys. Different kinds of superlattices can be distinguished by comparing the intensity ratios of the different reflections (I_{111}/I_{200}). The estimated value of the I_{111}/I_{200} ratio of the simulated pattern (Supporting Information, Fig.S2(a)) was found to be 0.83 and agrees closely with the experimentally observed values. This observation confirms the well-ordered $L2_1$ structure, i.e., no structural disorder in the present alloys was found during the investigation. It is observed that the intensity ratios for (111)/(200) decreases throughout the $Cu_2Mn_1Al_{1-x}Ga_x$ series with increasing x and reaches 0.80 for x = 0.28. It is worthwhile to mention that as Ga content increases, the peak intensity (at a higher angle) remarkably increases, which gives the signature of structural perfection on crystallization. This structural perfection (enhanced atomic ordering at their proper lattice sites) comes into play because of the larger atomic radius of Ga and half the surface energy in comparison to Al [51]. Thus, partial substitution of Al with Ga may lower the surface energy of the Cu-Mn-Al (Ga) alloy system. Moreover, it can be noticed from the inset of this

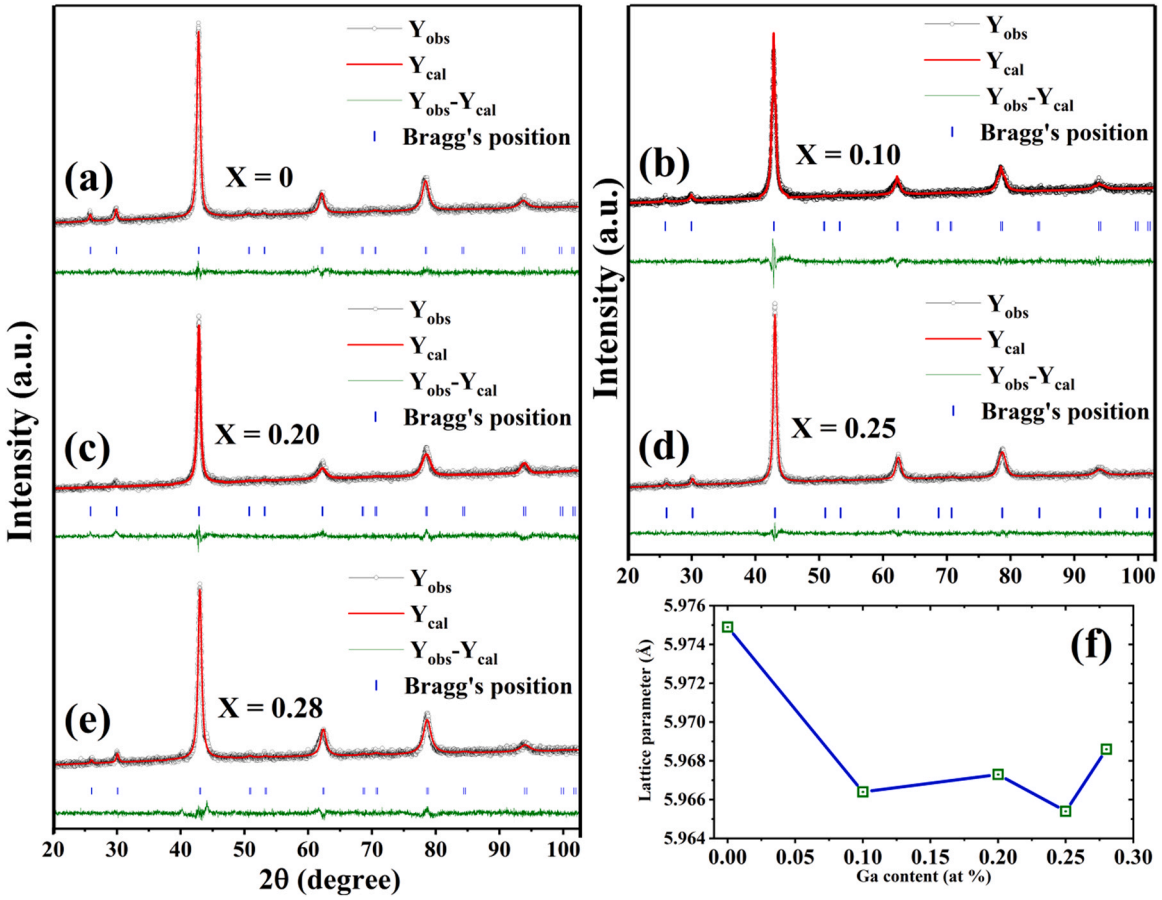

Fig. 1. Rietveld refinement of $Cu_2Mn_1Al_{1-x}Ga_x$ (a) x = 0 (b) x = 0.10, (c) x = 0.20, (d) x = 0.25 and (e) x = 0.28 Heusler alloys and (f) lattice parameter variation with Ga content.

figure that the (220) diffraction peak does shift with an increase in at % of Ga. The average crystallite size and lattice strain were estimated for all the alloys under investigation. Both crystallite size and strain do not follow any particular trend. The samples revealed this peculiar nature due to different valance state (+1, +3, +5) of the substituent (Ga).

The Reitveld analysis via fullProff software for $Cu_2Mn_1Al_{1-x}Ga_x$ (x = 0, 0.10, 0.20, 0.25, 0.28) alloys has been shown in Fig. 1. There is a good agreement between the observed (black) and calculated (red) positions of XRD diffraction profiles with high acceptability. The reliability factors were clearly found in the Rietveld refinement of XRD data, and the difference between the calculated and observed data has been shown by olive color Fig. 1(a–e). This confirms that all the samples under investigation were single-phase (i.e., no secondary phase was detected). The structure of all the alloys was the same except for a minimal difference in the angle of diffraction peaks. The lattice parameter 'a' for $0 \le x \le 0.28$ alloys was obtained from the refinement data, as shown in Fig. 1(f). This non-monotonic variation in the lattice parameter with Ga concentration can be explained based on the mixed valance states of Ga. There are three possible valance states of Ga, namely monovalent (Ga^{1+}), trivalent (Ga^{3+}) and pentavalent (Ga^{5+}). The atomic radius of Ga^{1+} is larger than the other two valance states, while the radius of Ga^{3+} and Ga^{5+} is equal to Al^{3+}. Thus, the non-linear increase in the lattice parameter could be explained if we assume the presence of a monovalent state of Ga. This indicates that some fraction of Ga atoms acquires the monovalent state during the crystallization.

The XRD pattern measured at room temperature for $Cu_2Mn_1Al_{1-x}Ga_x$ (x = 0.30, 0.40) alloys is shown in Fig. 2. The XRD patterns were found to have dual phase (HCP and complex cubic phases), Fig. 2(a, b). It is remarkable that as Ga concentration increased from 0.30 to 0.40, the peak intensity also increases with a reduction in the peak width, implying enhanced crystallinity, i.e., the constituents occupy the proper lattice sites and have less lattice strain. The Rietveld refinement results of calculated (red) XRD diffraction patterns are in good agreement with the observed (black) patterns, Fig. 2(c, d). The refinement and lattice parameters obtained after Rietveld refinement has been given in Table 1.

3.2. Morphological analysis

The surface morphology and phase evolution in the as-cast $Cu_2MnAl_{1-x}Ga_x$ (x = 0, 0.20, 0.40) alloys was examined using scanning electron microscopy (SEM). Fig. 3 shows the back scattered SEM images of $Cu_2MnAl_{1-x}Ga_x$ (x = 0, 0.20, 0.40) alloys. The absence of any color contrast in the back scattered images of the x = 0 and x = 0.2 samples (Fig. 3(a), (b)) indicate the formation of a single-phase ($L2_1$), whereas, in the case of the x = 0.4 alloy (Fig. 3(c)), two distinct contrasts (grey and white) were observed. The adjoining WDS compositional maps clearly show that x = 0 and x = 0.2 alloys (Fig. 3(a), (b)) have a single-phase microstructure with compositional homogeneity. On the other hand, the compositional variation for the two phases for the x = 0.4 sample is clearly evident from the corresponding compositional map in Fig. 3(c). The white region

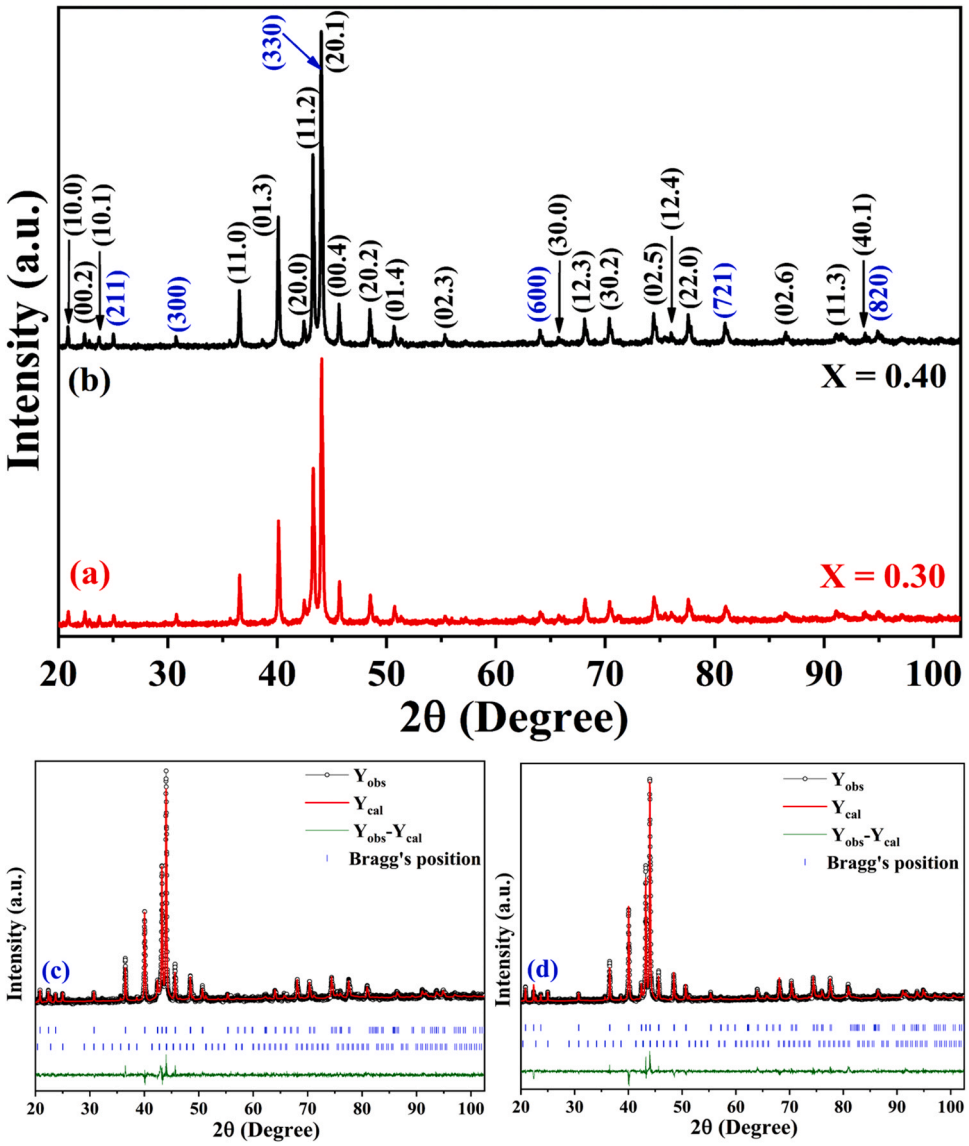

Fig. 2. XRD patterns of $Cu_2Mn_1Al_{1-x}Ga_x$Heusler alloys (a) x = 0.30, (b) x = 0.40 measured at room temperature, (c, d) Rietveld refinement of (a, b) respectively. Black and Blue indices correspond to HCP and γ-Cu_9Al_4 phases, respectively.

Table 1
Crystallite size, strain, and lattice parameters of $Cu_2Mn_1Al_{1-x}Ga_x$ (x = 0, 0.10, 0.20, 0.25, 0.28, 0.30, 0.40) Heusler alloys.

Composition	Sample	Crystallite Size (nm)	Lattice strain ($\times10^{-3}$)	a (Å)	c (Å)
Cu_2MnAl	x = 0	29.06	2.94	5.9749	–
$Cu_2Mn_1Al_{0.90}Ga_{0.10}$	x = 0.10	27.09	3.24	5.9664	–
$Cu_2Mn_1Al_{0.80}Ga_{0.20}$	x = 0.20	29.03	3.07	5.9673	–
$Cu_2Mn_1Al_{0.75}Ga_{0.25}$	x = 0.25	31.95	2.69	5.9654	–
$Cu_2Mn_1Al_{0.72}Ga_{0.28}$	x = 0.28	30.21	2.85	5.9686	–
$Cu_2Mn_1Al_{0.70}Ga_{0.30}$	x = 0.30	30.63	3.21	4.9202	7.9526
$Cu_2Mn_1Al_{0.60}Ga_{0.40}$	x = 0.40	27.69	3.55	4.9217	7.9557

(marked by yellow arrows in the inset of Fig. 3(c)) was found to be rich in Cu, whereas the grey region had less Cu content than the white region. This compositional difference denotes the formation of a dual-phase in the x = 0.4 alloy. It should be noted that the upper limits of the WDS color maps have been normalized as per the compositional distribution of Cu. These results were consistent with the XRD findings and optical microanalysis. The EDX analysis was used to estimate the purity of the samples, and the results are shown in Supporting Information, Fig. S3. The presence of elemental peaks associated only with constituents indicates the purity of the samples. Moreover, optical microscopy was used to probe the microstructural homogeneity of the samples and the results are summarized in Supporting Information, Fig. S4. The micrographs clearly show single phase, homogenous grains for the x = 0 and x = 0.2 alloys. This indicates that the x = 0 and x = 0.2 alloys crystalize into the $L2_1$ structure. The color contrast has been noticed due to the difference in the grain orientations. However, in the case of x = 0.4 alloy, two color contrasts within the same grain indicate the existence of dual phases in the as cast alloy, Fig. S4(c).

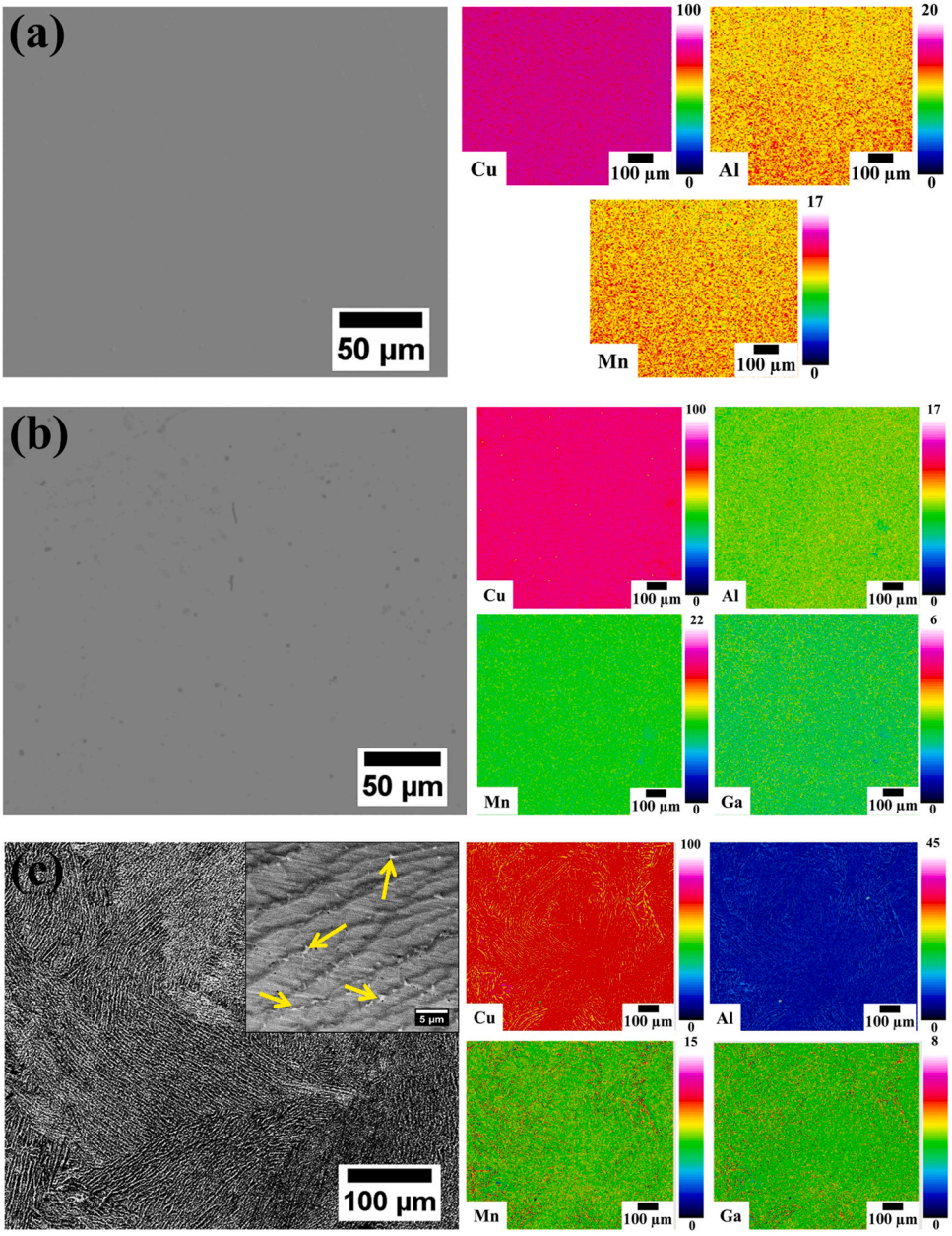

Fig. 3. SEM back scattered images and WDS compositional mapping for (d) x = 0, (e) x = 0.2, and (f) x = 0.4, Cu2Mn1Al1-xGax alloys respectively.

3.3. Microstructural investigation

In order to analyze the microstructure and phases of the $Cu_2Mn_1Al_{1-x}Ga_x$ (x = 0, 0.10, 0.20, 0.25, 0.28) Heusler alloys, extensive TEM investigation has been carried out. Fig. 4 presents the bright field (BF) TEM images and corresponding selected area (SAD) patterns along with intensity profiles of the respective SAD patterns. The microstructure of x = 0 alloy shows the random distribution of nanometer-sized grains in Fig. 4(a). The SAD pattern corresponding to Fig. 4(a) can be well indexed on the basis of the $L2_1$-type Heusler structure, as shown in Fig. 4(b). The TEM micrograph of the x = 0.10 sample has been shown in Fig. 4(d), which demonstrates the nanoparticles of arbitrary shapes and size, and the corresponding SAD pattern (Fig. 4(e)) was indexed as $L2_1$ structure with lattice parameter 5.95 Å. The high density of nanometer-sized grains for x = 0.28 alloy compared to the x = 0 and x = 0.10 alloys was evident from the microstructure in Fig. 4(g), and the corresponding SAD pattern gives the Debye-ring pattern, Fig. 4(h). The estimated D-values confirm the formation of the Cu_2MnAl Heusler phase. These results were consistent with XRD patterns that reveal the formation of the $L2_1$-type Heusler phase in this composition range. Fig. 4(c, f, i) presents the intensity profile (intensity vs. scattering/diffraction vector, k) that results from analyzing the respective SAD pattern using the Diffraction ring profile software. By azimuthal integration

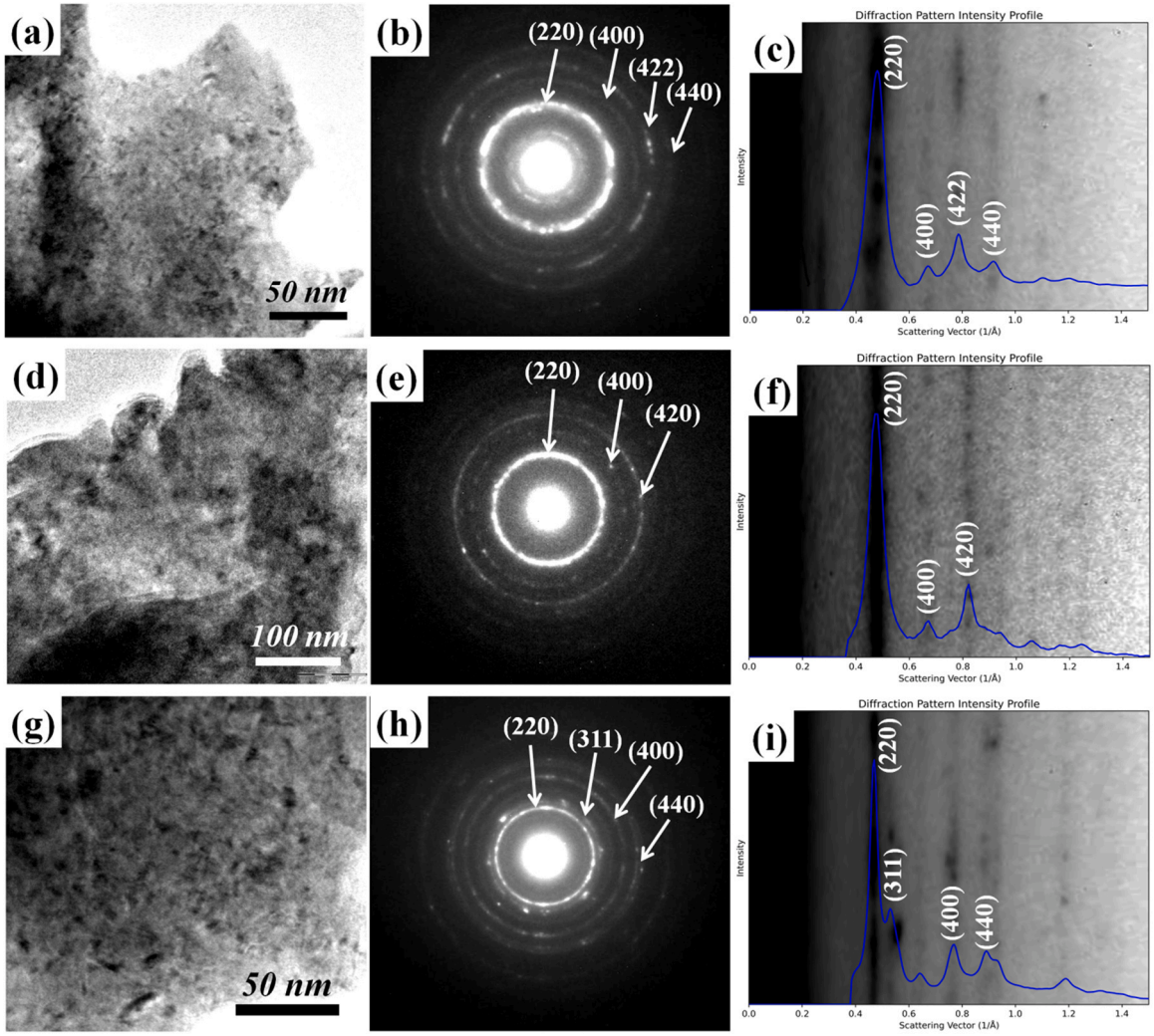

Fig. 4. TEM bright field image, corresponding SAD pattern and respective intensity profile of $Cu_2Mn_1Al_{1-x}Ga_x$ (a-c) x = 0, (d-f) x = 0.10 and (g-i) x = 0.28 Heusler alloys.

of the SAD ring patterns, these intensity profiles were deduced. The artificial peak broadening (even double peaks) was introduced because of the deviation from the correct center of integration. These intensity profiles were successfully indexed with the Cu_2MnAl Heusler phase.

The microstructural characterization of the $Cu_2MnAl_{1-x}Ga_x$ (x = 0.30, 0.40) Heusler alloys has been performed by TEM. Fig. 5 presents the TEM BF image, corresponding SAD pattern and respective intensity profiles of x = 0.30 and x = 0.40 alloys. In Fig. 5(a), nanometer-sized grains are clearly visible, and the corresponding SAD pattern provides a polycrystalline ring, Fig. 5(b). This ring pattern (Fig. 5(b)) was well indexed with Cu_3Mn_2Ga-type HCP and Cu_9Al_4-type cubic phases having lattice parameters a = 4.92 Å and c = 7.95 Å and a = 8.72 Å, respectively. The intensity profile obtained from Fig. 5(b) shows good congruence with the XRD results. Fig. 5(d, e) presents the microstructure and SAD pattern of x = 0.40 alloy. The SAD pattern is very sharp in this case, a signature of enhanced crystallinity, i.e., more structurally ordered than the previous alloy (x = 0.30). The lattice parameters estimated from the SAD pattern (Fig. 5(d)) for both phases are a = 4.92 Å, c = 7.96 Å and a = 7.96 Å, respectively. Fig. 5(f) shows the intensity profile of x = 0.40 alloy and is found to be consistent with XRD results.

3.4. Magnetic properties

The temperature-dependent magnetization (M-T) of Ga free and Ga substituted alloys were measured from 2 K to 300 K with zero-field cooled (ZFC) and field cooled (FC) protocols at 2 kOe and 5 kOe fields and are shown in Fig. 6. The bifurcation was observed in the ZFC and FC curves measured at 2 kOe in all the alloys at successively lower temperatures. This variation in the magnetization recorded in FC and ZFC modes comes into play due to the presence of short-range chemical disorders (because of Ga substitution) and anisotropy in the samples. Joy and Date [52] have reported that when the value applied field is higher than the coercivity for ferromagnetic material, a reduction in the magnetization was observed. Hence, the variation in magnetic behavior is attributed to domain wall pinning caused by anisotropy. At low temperatures, the magnetic moments do have enough energy to cross the anisotropy energy barrier, and therefore, the moment increases with a decrease in temperature,

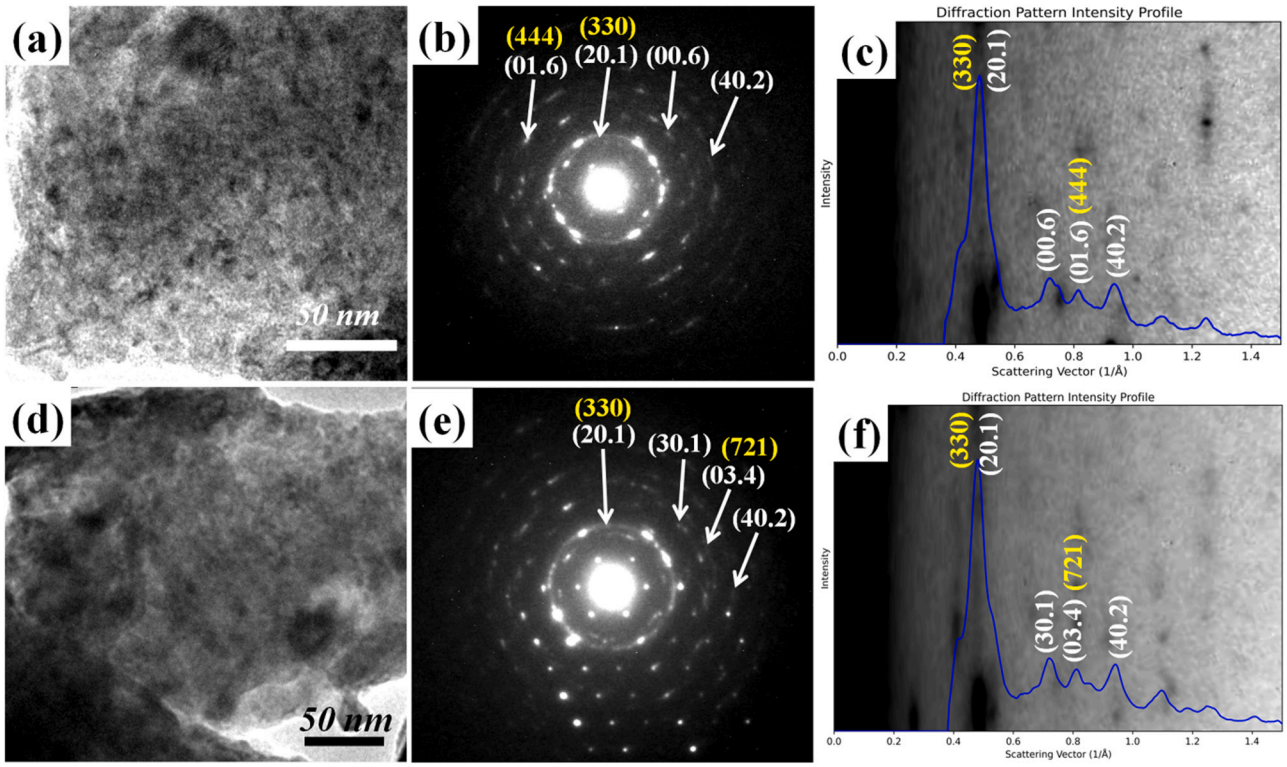

Fig. 5. TEM bright field image, corresponding SAD pattern and respective intensity profile of $Cu_2Mn_1Al_{1-x}Ga_x$ (a-c) x = 0.30 and (d-f) x = 0.40 Heusler alloys.

Fig. 6(a, c, e). It is clear from Fig. 6(a, c, e) that ferromagnetic (FM) to paramagnetic (PM) transition takes place at consecutive lower temperatures with an increase in Ga content, as the bifurcation was observed at successively lower temperatures for higher Ga concentration alloys. The magnetization curves as a function of $T^{3/2}$ are given in the inset of Supporting Information, Fig. S5 for the temperature range 50–200 K. These curves are following the relation $MT = M(0)(1\text{-}AT^n)$, where n = 1.5[53]. The linear fit (marked using solid lines) of the data determines the $T^{3/2}$ reliance of magnetization, attributing to the ferromagnetic nature of the alloys. This indicates that the ferromagnetic fraction is also present in the highest Ga content alloy, Supporting Information, Fig. S5(e, f).

These results indicate that magnetization depends upon the Ga concentration and the related phase(s) present in the alloys. At a higher applied field (5 kOe), the irreversibility in the magnetization ceased to an extent, particularly for x = 0 and 0.20 alloys, Fig. 6(b, d, f). However, there still exists a bifurcation in ZFC and FC curves of x = 0.40 sample (Fig. 6(f)) at a temperature lower than measured for the same alloy at the 2 kOe field (Fig. 6(e)). A monotonic variation in the magnetization at 2 kOe and 5 kOe (less than the saturation field limit) at the lower temperature range in both M-T curves of x = 0.40 alloy reveals the presence of short-range disordered magnetic entities Fig. 6(c, f). The parent and 5 at% Ga substituted alloy, Fig. 6(a, b), shows ferromagnetic nature/behavior due to the spin ordering of the moment of Mn atom into a canted state. For this composition (x = 0.40), canted antiferromagnetic Mn spins can be found. Mohan and Supanetz [54] have reported the moment of the Mn atom into a canted state at an angle of 60° in $Fe_{3-x}Mn_xSi$ Heusler alloys. Therefore, this low-temperature transition depends upon the magnitude of the applied field and chemical composition of the system and is defined as re-entrant temperature T_R. In the present investigation, T_R was found to shift to lower temperatures as the applied field increased from 2 kOe to 5 kOe, Fig. 6(c, f). Moreover, such a transition was absent for the alloys that crystalized into the $L2_1$ structure (x = 0, 0.20). The results show that the transition temperature T_R gets affected by the thermal history of magnetization. The FC curves of the x = 0.40 sample clearly reveal that the T_R changes from 8.2 K to 5.2 K, attributing to the irreversible nature of the transition. The applied magnetic field H restrains antiferromagnetic alignment and canting of Mn-spins and promotes the ferromagnetic alignment of the atomic spins. From the above observations, it is clear that the spin-canting phenomenon is independent of the magnitude of the externally applied field and chemical composition of alloy while it depends on the thermal history. The thermal history dependency of the spin-canting phenomenon was also reported for $Fe_{2-x}Co_xMnSi$ alloy [55].

To examine whether the substituents atoms are effectively occupying the proper lattice site or not, the isothermal magnetization M(H) were recorded by applying the external magnetic field up to 5 Tesla (50 kOe), at four different temperatures (10 K, 100 K, 200 K, and 300 K). The magnetization curves (M-H curves) are displayed in Fig. 7 for x = 0, 0.20 and 0.40 alloys. Similar M(H) signals were noticed in x = 0 and 0.20 alloys, demonstrating that the Ga atoms are effectively well substituted into the $L2_1$ lattice. In Cu_2MnAl Heusler alloy, the Mn atom has a large magnetic moment (about 3.0–4.0 μ_B) [53,56]. In the $L2_1$ lattice, the two Mn moments are coupled ferromagnetically when the Mn atoms reside at their proper position, or antiferromagnetic coupling occurs if Mn atoms go to the wrong site.

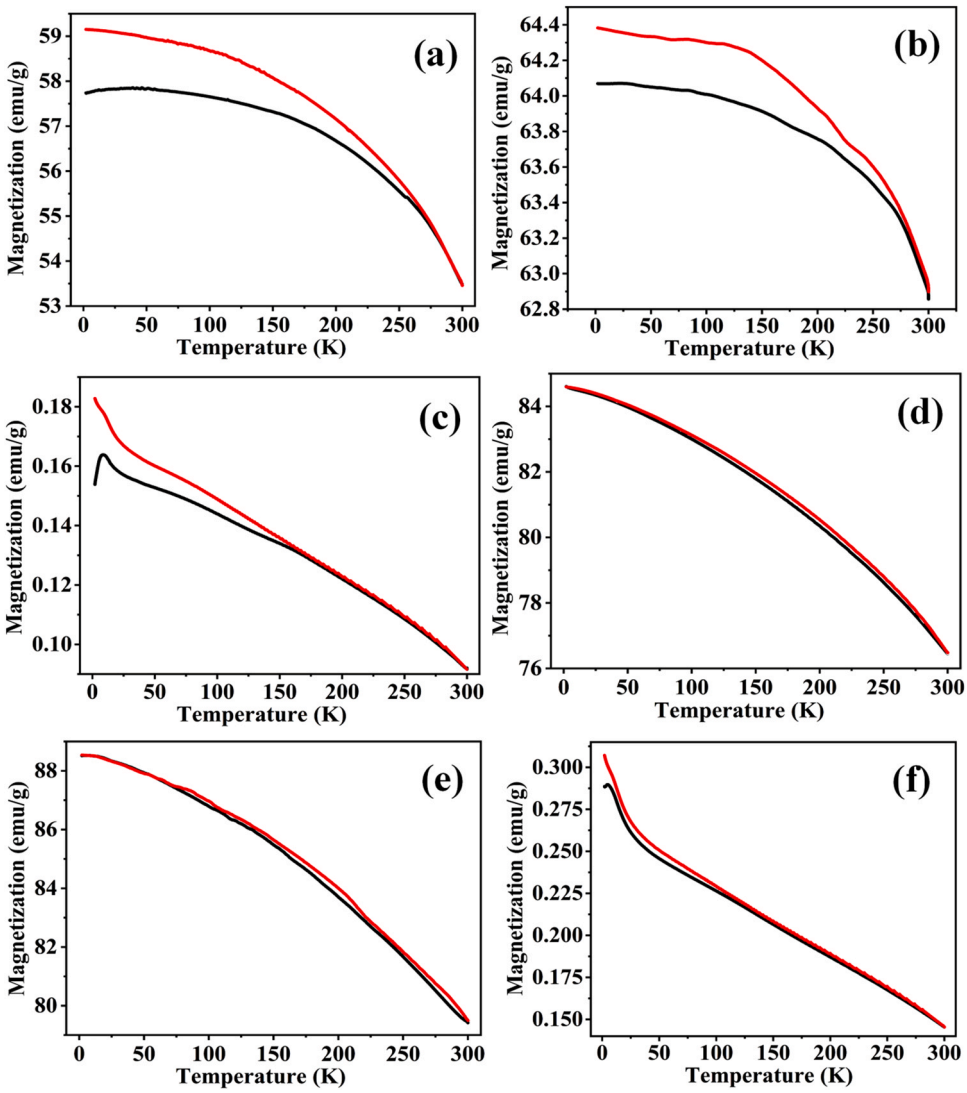

Fig. 6. Temperature dependence magnetization plots of $Cu_2Mn_1Al_{1-x}Ga_x$ Heusler alloys (a, b) x = 0, (c, d) x = 0.20 and (e, f) x = 0.40 recorded at 2 kOe and 5 kOe fields, respectively.

For the alloy of nominal composition Cu_2MnAl, the value of saturation magnetization (Ms) at 5 kOe decreases from 93.76 to 85.16 emu/gram with an increase in the temperature (10–300 K), Fig. 8(a). Similar values of Ms (92.18 – 84.54 emu/g) were observed for 5 at% Ga substituted alloy, Fig. 7(b). From Fig. 7(a, b), it can be observed that the magnetization starts saturating from a very low applied field, indicating that the alloys are fairly homogenous ferromagnets. The presence of negligible hysteresis shows that the alloys have soft ferromagnetic behavior at all the observed temperatures. The values of Ms for x = 0 and 0.20 alloys (93.76 and 92.18 emu/g respectively) at 10 K were found to be very close, as reported by Singh et al. [33]. In the alloys under investigation, only the concentration of Al was changed by partial substitution of Al with Ga, and the concentrations of Cu and Mn remained fixed in the $Cu_2Mn_1Al_{1-x}Ga_x$ alloy system. For the Cu_2MnAl alloy, the main contribution to the magnetic moment comes from the Mn-Mn interactions [53,56]. As discussed earlier, Ga substitution affects the lattice constant. The absence of any monotonic variation of the lattice parameters was attributed to Ga since it possesses multi-valence states. A negligible parameter change (0.007(6) Å) was noticed by 5 at% Al replacement. Therefore, the Mn–Mn distance in the lattice does not significantly change, thus, x = 0 and 0.20 alloys show similar nature, Fig. 7(a, b). However, magnetic properties get significantly influenced by Ga substitution in the ribbons of the same alloy [33]. Moreover, quite different nature of M-H curves was revealed by x = 0.40 alloy, as shown in Fig. 7(c) and will be discussed later.

It has been found that in the present study that some atoms of Ga possess a monovalent state along with a trivalent state, which gives rise to the non-monotonic variation in the lattice constant. Tobola et al. reported that the conduction electron helps in the magnetic exchange interaction [57]. It is obvious from the above discussion that the Mn atoms possessed the localized moment, and the conduction electrons were provided by the Al and Ga atoms. As the Ga content varied from 0 to 10 at%, it may be considered that magnetic properties were affected by the conduction electrons concentration. Hence, the substituent (Ga) mixed-valence states play a significant

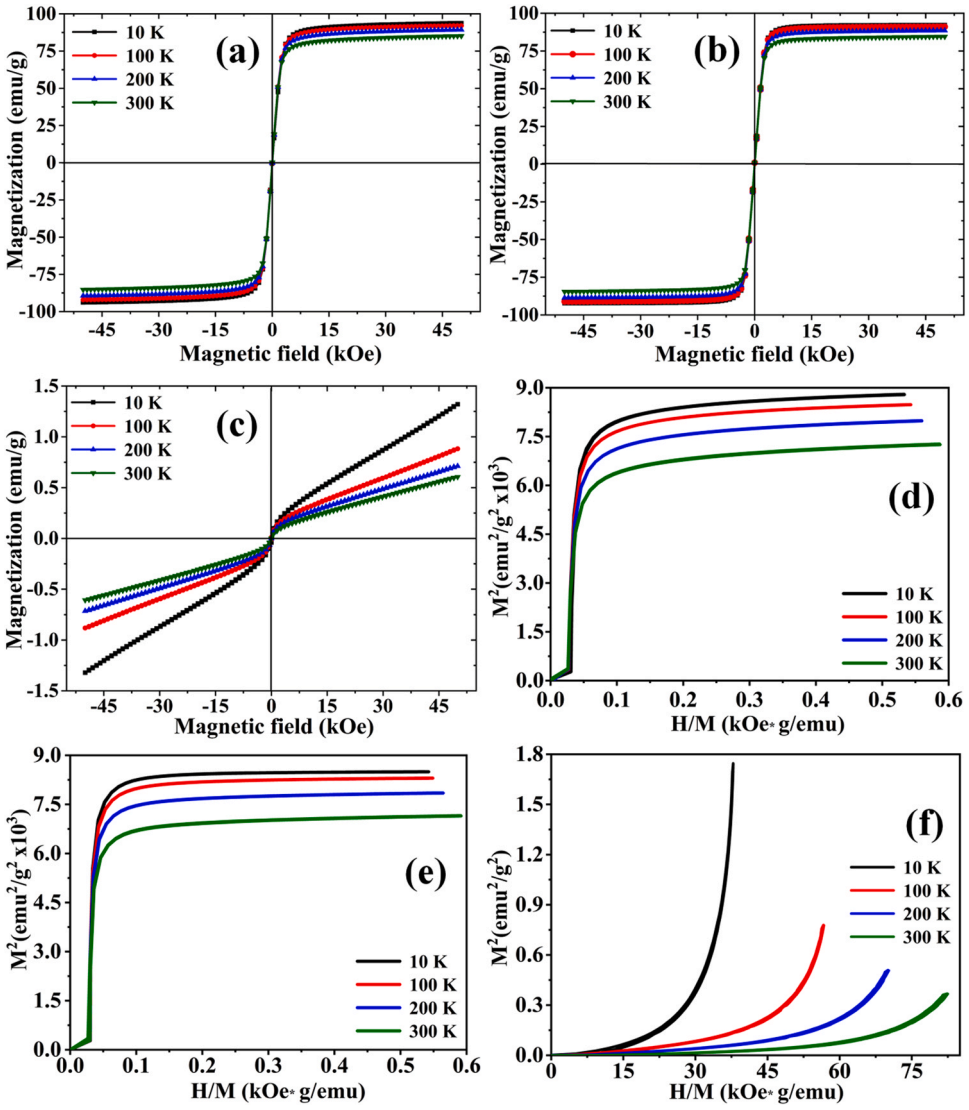

Fig. 7. The isothermal magnetization M versus field H curves of $Cu_2Mn_1Al_{1-x}Ga_x$ Heusler alloys (a) x = 0, (b) x = 0.20 and (c) x = 0.40 and (d-f) corresponding Arrott plots.

role in influencing the magnetic properties of the present alloy system. A few other factors, such as Ga content, the disordered occupation of Mn atoms, determine the magnetic properties because of the polarized conduction electrons involved in the magnetic exchange interactions. Hence, the concentration of the conduction electrons is supposed to be critical in fixing the crystal structure of the alloy [57]. The atomic concentration of Mn is fixed (25 at%) in the investigated material, so the magnetic properties of the alloys may be associated not only with Mn concentration but also with lattice site occupancy and the conduction electrons of Cu, Al, and Ga atoms.

Fig. 7(c) shows the diamagnetic nature of the alloy with nominal composition $Cu_2Mn_1Al_{0.60}Ga_{0.40}$. Initially, the magnetization abruptly increases in the lower field region, and by further increasing the applied field, the rate of moment increment gets reduced. Finally, the linear extension of magnetization was observed with increasing applied magnetic field and it does not get saturated even at the 50 kOe field, Fig. 8(c). These results recommend that there exist two possible components for this magnetization feature; (i) at low field region, readily magnetizing component, and (ii) at high field region, a non-saturating magnetic component [58,59]. Therefore, two magnetic phases are supposed to be present in this alloy. Along with the diamagnetic nature, the magnetic moment abruptly increases at lower fields, suggesting the presence of weak FM/AFM and/or PM counterparts [60]. The absence of the hysteresis indicates that the magnetic state is PM. This paramagnetic part comes from the γ-Cu_9Al_4 phase present in x = 0.40 alloy. As the temperature increases, the abrupt enhancing feature of magnetic moment at lower fields gets suppressed and at the higher field, the rate of paramagnetic magnetic moment increments also weakens, Fig. 7(c). This reduction in the values of the magnetic moment is caused probably due to strong magnetic anisotropy at higher temperatures. The unsaturated magnetic moment in the field up to 50 kOe indicates the existence of another magnetic ground state.

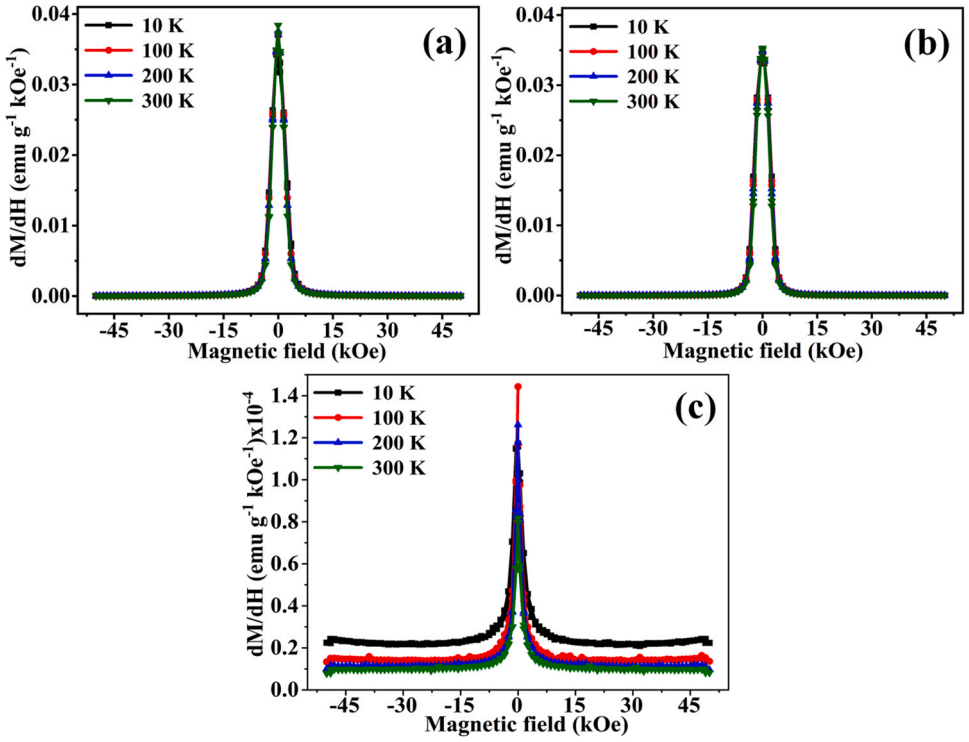

Fig. 8. Magnetic differential susceptibility curves as a function of magnetic field at different temperatures of $Cu_2Mn_1Al_{1-x}Ga_x$ Heusler alloys (a) x = 0, (b) x = 0.20 and (c) x = 0.40, respectively.

Further, to get a deeper insight into the magnetic properties and magnetic phase transitions in alloys, the Arrott plots were studied and are shown in Fig. 7(d–f). From the isothermal magnetization curves, the Arrott plots can be extracted. The Arrott curves are the plots between the ratio of the applied field (H/M) and the square of the magnetization (M^2) at a particular temperature and help determine the presence of ferromagnetic ordering in the sample. As per Banerjee's criterion [61], the sign (positive or negative) of the slope defines the type of magnetic phase transitions. The positive slope of the Arrott curves corresponds to the second-order magnetic phase transition, whereas the negative slope shows the transition is of the first order. In the present study, the Arrott plots corresponding to each sample exhibit a positive slope indicating a second-order FM to PM magnetic phase transition, Fig. 7(d–f). The differential magnetic susceptibility (dM/dH) plots (dM/dH versus H) help understand the magnetic feature affected by magnetic exchange interactions, illustrated in Fig. 8. They reveal the difference in terms of peak intensity and peak width. The peak of differential magnetic susceptibility curves coincides with the magnetic field strength at which the re-magnetization happens due to the polarity reversal in the material. A better interphase exchange coupling can be expected of the material if it exhibits a sharp peak, and if there exists an uncoupled soft and hard phase mixture, the presence of two distinct maxima is expected [62]. The x = 0 and x = 0.20 alloys show a similar nature (Fig. 8(a, b)), but the peak intensity of the first alloy was greater, indicating a better exchange coupling in Ga free alloy. It is also interesting to observe that at all the temperatures (10–300 K), the magnetic coupling remains unaffected in both alloys Fig. 8(a, b). Moreover, the peak intensity gets significantly reduced in x = 0.40 alloy (Fig. 8(c)), implying weaker exchange coupling between the magnetic phases. Hence, it can be concluded that the Ga substitution causes the reduction of exchange coupling. Recently, we have reported a similar type of exchange-coupling in Fe-based full Heusler alloys [38].

3.5. Lattice parameter modeling

The lattice parameter of a material is dependent on various parameters such as ionic radii, oxidation states, and electronegativity, which are a function of the inter-ionic distance. The ionic radii explain the role of geometry in the inter-ionic separation among atoms of the alloy. On the other hand, electronegativity accounts for the type of bonding among atoms. The strong connection between the lattice parameter and the inter-ionic distances explains the selection of these variables to be used for estimating the lattice parameter [63]. The lattice parameter for full Heusler alloys has been estimated through the GPR model in the present work. The training dataset for ml modeling is built to explore the non-linear relationship between the descriptors, which, then, can be modeled through the GPR model. The relationship between the descriptors used in the present study has been visualized for the training dataset in Supporting Information, Fig. S6.

3.5.1. Prediction accuracy and sensitivity

The final GPR model for the 262 chosen Heusler alloys is detailed visually in Fig. 9. Moreover, the predicted values of a_o for these alloys

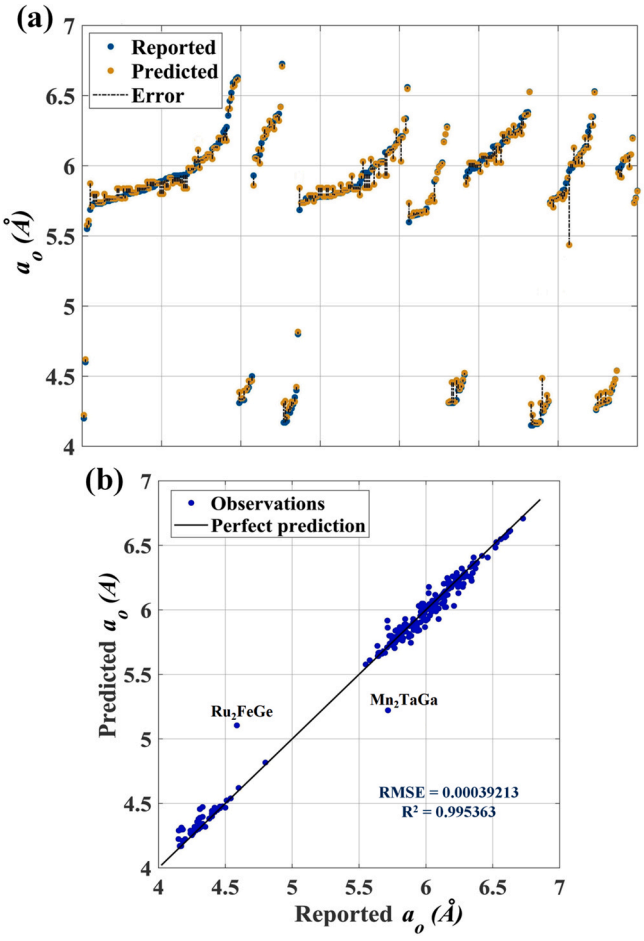

Fig. 9. (a) The reported and predicted a_o (Å) values for the 262 Heusler alloys taken in the training set using the GPR model; (b) The predicted vs. reported plot depicting efficiency of GPR model for a_o (Å) evaluation.

have been provided in Table 2. Fig. 9(a) shows a comparative plot between the estimated and theoretical values of the lattice parameter. It is evident from the figure as well as Table 2 that there exists good agreement among experimental and predicted values of a_o. Similar observations can be drawn from Fig. 9(b), where apart from two compositions (Ru_2FeGe and Mn_2TaGa), all other compositions show good symmetry along the perfect prediction diagonal line. The criteria used in the present study to evaluate the performance of the GPR model, i.e., the values of CC, MAE, and RMSE obtained through the model are 99.53%, 0.00033510 (0.0060% of the value of experimental average a_o (Å)), and 0.00039213 (0.0071% of the value of experimental average a_o (Å)), respectively. These represent the proposed GPR model showing good performance for the estimation of the lattice parameter of Heusler alloys. The training of the GPR model was also performed with various training datasets of different sizes extracted randomly from the input dataset to investigate the stability of the model in predicting lattice parameter. The variation in the MSE and RMSE values with training set size is shown in Supporting Information, Fig. S7. The values of both MAE and RMSE do not change significantly as the training set size increases from 26 to 260. This provides validation to the excellent stability of our ml model in predicting the lattice constant of Heusler alloys. It is worth mentioning that the training set for each training event was randomly selected from the whole dataset, including the alloys which appeared in the earlier training datasets.

Table 3 summarizes the prediction sensitivities of the proposed GPR model as a factor of the selection of kernels and basic functions. The table evidently highlights the emergence of the Exponential kernel as the ideal choice amongst the considered kernels. Moreover, the prediction outcomes are insensitive to the choice of basis function in the case of the Exponential kernel. Additionally, the table shows that the Empty basis function for the Exponential kernel causes a slight decrease in the model performance in comparison with the otherwise complex basis functions, namely, Constant, Linear, and Pure Quadratic. Nonetheless, the Empty basis function outcomes have been finally selected from the study due to its simplicity, which can play a substantial role in the generalization of the proposed model. Thus, the model shows great stability and accuracy, leading to accurate lattice constant (a_o) estimation for Heusler alloys. More importantly, the estimation of a_o through the present model is based on the basic properties of the alloying elements, i.e., the ionic radii and electronegativity, which makes the model versatile.

3.5.2. *Prediction of lattice parameters variation with Ga substitution in $X_2YAl_{1-x}Ga_x$ alloys*

The variations in the lattice parameter of an alloy greatly depend upon the ionic radii, valence, and electronegativities of the constituents [63,64]. The ionic radius, dependent on the type of element, its coordination number, and oxidation state, fundamentally plays a crucial role in describing the crystal structure from a geometric viewpoint. Electronegativity is another factor that performs a significant role in defining the crystal structure by determining the degree of the ionic character of the bond [65]. Thus, when explained using the ionic radii and electronegativity, the lattice parameter can provide an accurate picture of the crystal structure of Heusler alloys. The developed GPR model has been used to estimate the lattice parameter for a series of Heusler alloys in the present study. Notably, the lattice parameter value change on the substitution of Al with Ga in the Heusler alloys has been studied. Several pairs of such substitutions and the reported and predicted lattice parameter values have been marked in blue in Table 2. Of these, 13 such pairs have been studied with the GPR model to show the variation in their lattice parameter through progressive substitution of Al with Ga. The estimated values of the lattice parameter through the GPR model for these 13 compositions have been shown in Fig. 10(a). As evident from Fig. 10(a) and Table 2, the substitution of Al atoms with Ga atoms leads to an increase in the lattice parameter and expansion of the size of the lattice since Ga atoms are much larger in comparison to Al. However, in a few cases, namely $Co_2Hf_1Al_{1-x}Ga_x$ and $Cu_2Mn_1Al_{1-x}Ga_x$, the substitution shows an inverse effect on the lattice parameter due to the dynamic nature of the valence of Ga, which transforms from trivalent (Ga^{3+}) or pentavalent (Ga^{5+}) to monovalent (Ga^{1+}) for these alloys. In particular, the estimated values of the lattice parameter and their trend for the substitution of Al with Ga for $Cu_2Mn_1Al_{1-x}Ga_x$ illustrated in Fig. 10(b) coincides with the experimental values illustrated in Fig. 1(f) and Table 1. An important observation is the non-monotonic nature of lattice parameter variation with increasing Ga concentration which can be explained on the basis of the mixed valance states of Ga. Thus, the non-linear change in the lattice parameter is explained by the

Table 2
Reported and predicted lattice parameters of full Heusler alloys using GPR model (Input parameters and references are provided with source information in Supplementary Information ST1).

Alloy	a_o (Å) (Reported)	a_o (Å) (Predicted)	Alloy	a_o (Å) (Reported)	a_o (Å) (Predicted)
Au2MnAl	6.462	6.406	Fe2MnGe	5.789	5.800
Au2MnGa	6.560	6.548	Fe2MnAl	5.830	5.845
Au2MnIn	6.726	6.708	Fe2MnGa	6.006	6.015
Au2MnSi	6.512	6.516	Fe2MnSn	6.142	6.144
Au2MnGe	6.594	6.530	Fe2MnIn	6.197	6.201
Au2MnSn	6.831	6.827	Fe2MoSn	4.310	4.457
Co2CrAl	5.727	5.730	Fe2MoSb	4.310	4.389
Co2CrGa	5.805	5.807	Fe2MoAl	5.918	5.914
Co2CrIn	6.060	6.053	Fe2NiSi	5.648	5.660
Co2CuAl	5.550	5.577	Fe2NiAl	5.758	5.766
Co2FeSi	5.640	5.642	Fe2NiGa	5.780	5.780
Co2FeAl	5.730	5.739	Fe2NiGe	5.771	5.762
Co2FeGa	5.737	5.735	Fe2TiGe	5.740	5.728
Co2HfAl	6.020	6.037	Fe2TiAs	5.740	5.734
Co2HfGa	6.030	6.025	Fe2TiGa	5.800	5.789
Co2HfSn	6.220	6.217	Fe2TiAl	5.879	5.875
Co2MnSi	5.694	5.667	Fe2TiSb	6.000	5.917
Co2MnGe	5.749	5.762	Fe2TiSn	6.030	5.956
Co2MnAl	5.776	5.768	Fe2TiIn	6.060	6.048
Co2MnGa	5.873	5.789	Fe2VAl	5.761	5.765
Co2MnSb	5.982	5.920	Fe2VGa	5.782	5.783
Co2MnSn	6.000	6.009	Fe2VSn	5.959	5.904
Co2MnIn	6.078	6.016	Fe2WSb	4.320	4.323
Co2MoGa	4.170	4.308	Fe2MoGa	4.14	4.154
Co2MoGe	4.180	4.309	Fe2WGa	4.15	4.150
Co2MoSb	4.320	4.334	Fe2MoGe	4.15	4.147
Co2MoIn	4.330	4.343	Fe2WIn	4.3	4.294
Co2MoSn	4.330	4.473	Fe2MoIn	4.3	4.297
Co2NbAl	5.935	5.838	Fe2WSn	4.31	4.295
Co2NbGa	5.950	5.842	Fe2CrV	5.71	5.714
Co2NbSn	6.142	6.021	Ir2VGa	6.009	6.007
Co2OsGe	4.160	4.168	Ir2MnAl	6.022	6.178
Co2OsSb	4.300	4.302	Ir2VGe	6.054	6.051
Co2OsSn	4.310	4.322	Mn2MoGe	4.150	4.151
Co2RuGe	4.150	4.224	Mn2WGe	4.160	4.169
Co2RuSb	4.290	4.358	Mn2CrAl	5.710	5.709
Co2RuIn	4.310	4.387	Mn2CrGa	5.770	5.745
Co2ScGe	5.780	5.769	Mn2CrSb	5.980	5.948
Co2ScGa	6.170	6.162	Mn2MoGa	4.170	4.324
Co2ScSn	6.190	6.178	Mn2MoSb	4.300	4.379
Co2TaAl	5.930	5.887	Mn2MoSn	4.310	4.456
Co2TiSi	5.743	5.742	Mn2MoIn	4.330	4.396
Co2TiGe	5.807	5.781	Mn2NbGa	6.013	5.929
Co2TiAl	5.850	5.847	Mn2TaGa	6.210	6.031
Co2TiGa	5.856	5.858	Mn2TiSi	5.783	5.788
Co2TiSn	6.070	6.049	Mn2TiAs	5.822	5.818
Co2VGe	5.766	5.703	Mn2TiGe	5.876	5.814
Co2Vas	5.772	5.766	Mn2TiGa	5.987	6.031
Co2VGa	5.792	5.842	Mn2TiAl	5.967	5.962
Co2VAl	5.847	5.838	Mn2TiSb	6.075	5.988
Co2VSn	5.980	6.021	Mn2TiSn	6.136	6.062
Co2WGe	4.170	4.170	Mn2VAl	5.687	5.687
Co2WSb	4.310	4.311	Mn2VGa	5.905	5.929
Co2WSn	4.320	4.319	Mn2VSn	5.920	5.866
Co2ZrAl	6.080	6.083	Mn2VIn	5.930	5.859
Co2ZrSn	6.242	6.238	Mn2VGe	6.095	6.010
Co2RuGa	4.15	4.158	Mn2WGa	4.180	4.210
Co2WGa	4.16	4.169	Mn2WSn	4.310	4.315
Co2OsGa	4.16	4.158	Mn2WSb	4.310	4.331
Co2FeSb	4.22	4.227	Mn2WIn	4.330	4.342
Co2MnSb	4.25	4.242	Mn2ZrSi	6.004	6.002
Co2RuSn	4.3	4.308	Mn2ZrGe	6.086	6.081
Co2Win	4.31	4.311	Mn2VSi	5.56	5.562
Co2OsIn	4.31	4.316	Mn2CrSi	5.59	5.602
Co2FeGe	5.738	5.739	Mn2VGe	5.65	5.651
Co2CrV	5.76	5.763	Mn2CrGe	5.73	5.740
Cr2FeSb	6.040	6.039	Ni2CoAl	4.200	4.224
Cr2CoSb	6.060	6.061	Ni2CoGa	4.400	4.414
Cr2NiSb	6.080	6.080	Ni2CoGe	4.300	4.366
Cu2CrAl	5.809	5.809	Ni2CrAl	5.737	5.740
Cu2MnAl	5.978	5.976	Ni2CuAl	5.580	5.609
Cu2MnGa	5.970	5.973	Ni2FeSb	4.260	4.271
Cu2MnSi	5.993	5.990	Ni2FeAl	4.600	4.620
Cu2MnGe	6.114	6.106	Ni2FeGa	4.800	4.817

(*continued on next page*)

Table 2 (*continued*)

Alloy	a_o (Å) (Reported)	a_o (Å) (Predicted)	Alloy	a_o (Å) (Reported)	a_o (Å) (Predicted)
Cu2MnIn	6.200	6.259	Ni2MnAl	5.824	5.844
Cu2MnSn	6.342	6.225	Ni2MnGa	5.835	5.866
Fe2WGe	4.160	4.172	Ni2MnGe	5.909	5.914
Fe2CoSi	5.645	5.642	Ni2MnIn	6.070	6.116
Fe2CoGa	5.767	5.744	Ni2MnSb	6.027	6.046
Fe2CrSi	5.679	5.679	Ni2MnSi	5.766	5.774
Fe2CrAl	5.810	5.809	Ni2MnSn	6.048	6.072
Fe2CrGa	5.824	5.828	Ni2CoSi	3.95	4.103
Fe2MnSi	5.672	5.669	Ni2FeSi	4	4.006
Ni2FeSn	4.25	4.248	Ni2CoSb	4.2	4.188
Ni2FeGe	4.8	4.783	Ni2CoSn	4.21	4.205
Pd2CoGa	4.300	4.314	Rh2FeSn	6.842	6.843
Pd2CoGe	4.320	4.325	Ru2FeGa	4.240	4.268
Pd2CoIn	4.460	4.463	Ru2FeGe	4.240	5.105
Pd2CoSn	4.460	4.476	Ru2FeIn	4.400	4.399
Pd2CoSb	4.480	4.478	Ru2FeSn	4.400	4.442
Pd2FeSn	4.510	4.524	Ru2FeSb	4.400	4.423
Pd2FeSb	4.540	4.539	Ru2HfSn	6.382	6.366
Pd2MnAl	6.165	6.200	Ru2MnSi	5.887	5.745
Pd2MnGa	6.332	6.332	Ru2MnAl	6.054	6.052
Pd2MnIn	6.268	6.321	Ru2MnGa	6.138	6.136
Pd2MnGe	6.282	6.202	Ru2MnGe	6.066	6.013
Pd2MnSi	6.172	6.168	Ru2MnSb	6.200	6.194
Pd2MnSn	6.350	6.361	Ru2MnIn	6.281	6.273
Pd2FeGe	4.36	4.364	Ru2MnSn	6.284	6.250
Pd2MnSb	6.42	6.437	Ru2TiSi	5.958	5.953
Pt2MnGa	6.160	6.247	Ru2TiGe	6.035	6.009
Pt2MnSi	6.224	6.225	Ru2TiSn	6.241	6.216
Pt2MnAl	6.240	6.178	Ru2VSi	5.904	5.902
Pt2MnIn	6.254	6.253	Ru2VGa	5.989	5.971
Pt2MnGe	6.348	6.350	Ru2VSn	6.190	6.174
Pt2MnSn	6.527	6.525	Ru2MnSb	6.2009	6.194
Rh2CoGa	4.240	4.290	Sc2CoSi	6.280	6.271
Rh2CoGe	4.250	4.254	Sc2CoGe	6.350	6.286
Rh2CoSb	4.380	4.383	Sc2CuAl	6.520	6.482
Rh2CoIn	4.400	4.417	Sc2CrGe	6.530	6.521
Rh2CoSn	4.400	4.407	Sc2CrSi	6.58	6.591
Rh2CrAl	6.063	6.054	Sc2CoSn	6.62	6.617
Rh2CrGa	6.098	6.091	Sc2CrSn	6.95	6.950
Rh2CrIn	6.293	6.291	Ti2CuAl	6.130	6.126
Rh2CuSn	6.144	6.107	Ti2CoGa	6.120	6.107
Rh2FeGe	4.280	4.291	Ti2FeGa	6.120	6.105
Rh2FeGa	4.350	4.319	Ti2FeAl	6.140	6.128
Rh2FeSn	4.420	4.433	Ti2CoAl	6.140	6.125
Rh2FeSb	4.440	4.449	Ti2NiGa	6.190	6.188
Rh2FeIn	4.500	4.468	Ti2NiAl	6.200	6.195
Rh2MnAl	5.980	6.048	Ti2FeIn	6.230	6.221
Rh2MnGa	6.210	6.202	Ti2CoIn	6.360	6.346
Rh2MnSi	6.023	6.013	Ti2NiIn	6.420	6.419
Rh2MnGe	6.020	6.129	Zr2MnAl	6.590	6.562
Rh2MnSn	6.230	6.286	Zr2FeAl	6.600	6.571
Rh2MnIn	6.352	6.344	Zr2CoAl	6.621	6.605
Zr2NiAl	6.630	6.623	Zr2CoGa	6.588	6.593
Zr2CrAl	6.66	6.665	Zr2CoIn	6.797	6.782
Zr2NbIn	6.9	6.933	Zr2NbAl	6.8	6.801
			Zr2NbGa	6.74	6.752
Correlation Coefficient					0.995363
Mean Absolute Error					0.0028563
Root Mean Square Error					0.0003921

Table 3
The prediction sensitivities of GPR model based on the choices of kernels and basis functions.

Kernel	Basis function	CC (%)	RMSE	RMSE		MAE	MAE	
				Sample	Mean		Sample	Mean
Exponential	Constant	99.68	0.00038076	0.0068%		0.00029412	0.0053%	
Exponential	Empty	99.53	0.00039213	0.0071%		0.00033510	0.0060%	
Exponential	Linear	99.68	0.00038163	0.0038%		0.00029592	0.0053%	
Exponential	Pure quadratic	99.62	0.00025886	0.0069%		0.00036092	0.0065%	
Squared exponential	Empty	78.2	0.25385138	4.574723%		0.19068259	3.4346342%	
Matern 5/2	Empty	79.6	0.23294689	4.197997%		0.18038060	3.2506866%	
Rational quadratic	Empty	78.8	0.24868538	4.481625%		0.19068259	3.4363415%	

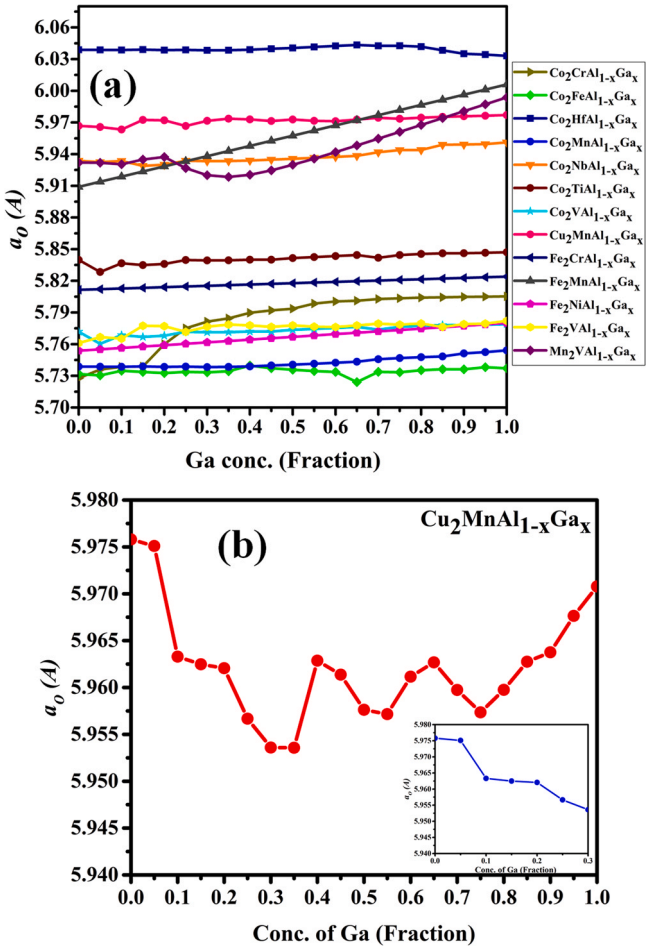

Fig. 10. Prediction of lattice parameter variation with Ga substitution at Al site in (a) various full-Heusler alloys, (b) $Cu_2Mn_1Al_{1-x}Ga_x$ alloy.

presence of a fraction of monovalent Ga atoms along with the trivalent and pentavalent Ga atoms [41].

4. Conclusions

The present work involves investigating the effect of Ga substitution on the structural and magnetic properties in Cu_2MnAl full Heusler alloy. The formation of a body-centered (BCC) based superstructure was identified by indexing the characteristic, and the superlattice reflections corresponding to the parent alloy confirm an ordered $L2_1$ structure. This $L2_1$ phase was found to be stable up to the Ga concentration of 0.28 alloy. It, subsequently, transformed into two phases consisting of an HCP and simple cubic gamma brass type complex structure with an increase of the Ga content to 0.30. The non-linear variation of the lattice constant was attributed to the monovalent state of Ga. The crystallite size and lattice strain were found to vary non-monotonically with the increase in the Ga concentration, and the alloy $x = 0.40$ exhibited the largest strain (3.55×10^{-3}). The saturation magnetization of $x = 0$ and $x = 0.30$ alloys were approximately equal, but these alloys have larger ferromagnetic fraction in comparison with $x = 0.40$ alloy. A second-order magnetic phase transition (ferromagnetic to paramagnetic transition) was observed. The investigation of the Arrott plots also confirmed this magnetic transition. The Ga substitution was found to be responsible for weakening the magnetic exchange coupling between the magnetic phases. Furthermore, the estimation of the lattice parameter for Heusler alloys was attempted using machine learning. A good correlation among the experimental and predicted a_o (Å), with extremely low error, and the insensitivity of the proposed model to changing algorithm functions indicate the suitability of GPR in modeling and recognizing the correlation amongst the physical features of the alloying elements and the lattice parameter of the alloys. The developed model is uncomplicated and versatile, which can also be used to design new Heusler alloy systems as functional materials having desired lattice constants.

CRediT authorship contribution statement

Shashank Shekhar Mishra: Conceptualization, Synthesis, experimentation, sample characterization, writing. **Anurag Bajpai:** calculations, machine learning model development, analysis of simulation results, writing. **Ram Manohar Yadav:** Magnetic measurements, Supervision and review of manuscript. **Anand B. Puthirath:** Magnetic measurements. **Liangzi Deng:** Magnetic measurements. **Moein Adnani:** Magnetic measurements. **Ching-Wu Chu:** Magnetic measurements. **Robert Vajtai:** Magnetic measurements. **Thakur Prasad Yadav:** Supervision and review of manuscript. **Pulickel M Ajayan:** Supervision and review of manuscript. **Krishanu Biswas:** Supervision and review of manuscript. **Nilay Krishna Mukhopadhyay:** Supervision and review of manuscript.

Declaration of Competing Interest

The authors declare that they have no known competing financial interests or personal relationships that could have appeared to influence the work reported in this paper.

Acknowledgment

S. S. Mishra thanks the University Grants Commission (UGC), India, for the BSR fellowship, during which period the work was completed. RMY acknowledges the United States-India Educational Foundation (USIEF) and Fulbright Foreign Scholarship Board (FFSB), USA, for Fulbright Nehru Academic and Professional Excellence Fellowship. The work performed at the Texas Center for Superconductivity at the University of Houston is supported by the U.S. Air Force Office of Scientific Research Grant FA9550-15-1-0236, the T. L. L. Temple Foundation, the John J. and Rebecca Moores Endowment, and the State of Texas through the Texas Center for Superconductivity at the University of Houston. S.S.M. acknowledges Ms. Khushubo Tiwari for encouraging discussions while preparing the manuscript. A.B.P. acknowledges IUSSTF and SERB India for financial support in the form of the postdoctoral fellowship.

Author contributions

S.S.M. synthesized the series of alloys, performed the experiments, and subsequently performed the XRD, SEM, EDX, and TEM characterizations. R.M.Y, A.B.P., L.Z.D., M.A., C.W.C., and R.V. performed the magnetic measurements. A.B. performed calculations, developed the machine learning model, analyzed and plotted the simulation results. T.P.Y., R.M.Y, P.M.A, K.B., N.K.M. supervised and participated in the discussion of results. S.S.M. and A.B. organized the data and wrote the manuscript. All the authors reviewed and contributed to the final draft of the manuscript.

Appendix A. Supporting information

Supplementary data associated with this article can be found in the online version at doi:10.1016/j.jallcom.2021.162865.

References

[1] S. Mishra, S. Mukhopadhyay, T. Yadav, R. Yadav, R. Romero-Aburto, R. Vajtai, P. Ajayan, N. Mukhopadhyay, O. Srivastava, Structural and magnetic properties of rapidly solidified Ni45Fe5Mn40Sn10 alloy ribbon, J. Adv. Phys. 6 (2017) 389–396.

[2] J. Winterlik, S. Chadov, A. Gupta, V. Alijani, T. Gasi, K. Filsinger, B. Balke, G.H. Fecher, C.A. Jenkins, F. Casper, Design scheme of new tetragonal Heusler compounds for spin-transfer torque applications and its experimental realization, Adv. Mater. 24 (2012) 6283–6287.

[3] A. Hirohata, K. Takanashi, Future perspectives for spintronic devices, J. Phys. D: Appl. Phys. 47 (2014) 193001.

[4] S. Mishra, S. Mukhopadhyay, T. Yadav, R. Yadav, S. Radhakrishnan, R. Vajtai, P. Ajayan, N. Mukhopadhyay, H. Singh, O. Srivastava, Effect of Fe substitution by Co on off-stoichiometric Ni–Fe–Co–Mn–Sn Heusler alloy ribbons, Mater. Res. Express 4 (2017) 086507.

[5] Y. Zhang, W. Zhang, X. Yu, C. Yu, Z. Liu, G. Wu, F. Meng, The structural, magnetic and electronic properties of Fe-Ni-Ga ternary Heusler alloys, Mater. Sci. Eng.: B 260 (2020) 114654.

[6] R.S. Sunmonu, J.O. Akinlami, E.O. Dare, G.A. Adebayo, DFT – GGA calculations of magnetic, elastic, thermodynamic and thermoelectric properties of Co2YAl (Y = Ti, V) full Heusler alloy systems, Mater. Sci. Eng.: B 262 (2020) 114739.

[7] A. Yari, M. Yeganeh, F.M. Dezfuli, A. Boochani, Investigation of the stability, electronic structure, and magnetic properties of Sc2VZ (Z = Ge, Si) Heusler alloys: first-principles calculations, Mater. Sci. Eng.: B 267 (2021) 115096.

[8] P. Villars, L. Calvert, Pearson's Handbook of Crystallographic Data for Intermediate Phases, American Society of Metals, Cleveland, OH, 1985.

[9] D.C. Gupta, I.H. Bhat, Investigation of high spin-polarization, magnetic, electronic and half-metallic properties in RuMn2Ge and RuMn2Sb Heusler alloys, Mater. Sci. Eng.: B 193 (2015) 70–75.

[10] D. Rai, A. Shankar, M. Ghimire, R. Thapa, Electronic and magnetic properties of a full-Heusler alloy Co 2 CrGe: a first-principles study, J. Theor. Appl. Phys. 7 (2013) 3.

[11] Y. Jin, P. Kharel, P. Lukashev, S. Valloppilly, B. Staten, J. Herran, I. Tutic, M. Mitrakumar, B. Bhusal, A. O'Connell, Magnetism and electronic structure of CoFeCrX (X= Si, Ge) Heusler alloys, J. Appl. Phys. 120 (2016) 053903.

[12] S. Wolf, D. Awschalom, R. Buhrman, J. Daughton, vs. von Molnár, M. Roukes, A.Y. Chtchelkanova, D. Treger, Spintronics: a spin-based electronics vision for the future, Science 294 (2001) 1488–1495.

[13] S. Yousuf, D.C. Gupta, Investigation of spin polarized band structure, magnetism, and mechanical properties of new gapless Zr2NbX (X= Al, Ga, In) Heusler alloys, J. Alloy. Compd. 766 (2018) 241–247.

[14] M.K. Hussain, Investigations of the stability, electronic and magnetic structures in the Zr2Ni-based Heusler compounds: first principles study, Mater. Sci. Eng.: B 264 (2021) 114922.

[15] N. Nishizawa, H. Munekata, Efficient spin injection through a crystalline AlO x tunnel barrier prepared by the oxidation of an ultra-thin Al epitaxial layer on GaAs, J. Appl. Phys. 114 (2013) 033507.

[16] Y. Koshkid'ko, S. Pandey, J. Cwik, I. Dubenko, A. Aryal, A. Granovsky, D. Szymanski, S. Stadler, E. Lähderanta, N. Ali, Relaxation phenomena in adiabatic temperature changes near magnetostructural transitions in Heusler alloys, J. Alloy. Compd. 821 (2020) 153402.

[17] T. Kimura, N. Hashimoto, S. Yamada, M. Miyao, K. Hamaya, Room-temperature generation of giant pure spin currents using epitaxial Co 2 FeSi spin injectors, NPG Asia Mater. 4 (2012) e9.

[18] K. Kasahara, Y. Fujita, S. Yamada, K. Sawano, M. Miyao, K. Hamaya, Greatly enhanced generation efficiency of pure spin currents in Ge using Heusler compound Co2FeSi electrodes, Appl. Phys. Express 7 (2014) 033002.

[19] F. Yang, C. Wei, X. Chen, Half-metallicity and anisotropic magnetoresistance of epitaxial Co2FeSi Heusler films, Appl. Phys. Lett. 102 (2013) 172403.

[20] T. Graf, F. Casper, J. Winterlik, B. Balke, G.H. Fecher, C. Felser, Crystal structure of new Heusler compounds, Z. für Anorg. und Allg. Chem. 635 (2009) 976–981.

[21] D. Erb, G. Nowak, K. Westerholt, H. Zabel, Thin films of the Heusler alloys Cu2MnAl and Co2MnSi: recovery of ferromagnetism via solid-state crystallization from the x-ray amorphous state, J. Phys. D: Appl. Phys. 43 (2010) 285001.

[22] C. Grigorescu, E. Valerio, O. Monnereau, L. Tortet, L. Argeme, G. Pavelescu, S. Manea, C. Ducu, A. Malinovski, H. Trodahl, Pulsed laser deposition of Co-based Tailored-Heusler alloys, Appl. Surf. Sci. 253 (2007) 8102–8106.

[23] R. Topkaya, R. Yilgin, S. Kazan, N. Akdoğan, M. Obaida, H. Inam, K. Westerholt, Annealing effect on structural and magnetic properties of Cu 2 MnAl Heusler alloy films, J. Supercond. Nov. Magn. 25 (2012) 2605–2609.

[24] M. Jourdan, J. Minár, J. Braun, A. Kronenberg, S. Chadov, B. Balke, A. Gloskovskii, M. Kolbe, H.-J. Elmers, G. Schönhense, Direct observation of half-metallicity in the Heusler compound Co 2 MnSi, Nat. Commun. 5 (2014) 1–5.

[25] S. Skaftouros, K. Özdoğan, E. Şaşıoğlu, I. Galanakis, Generalized Slater-Pauling rule for the inverse Heusler compounds, Phys. Rev. B 87 (2013) 024420.

[26] Y. Sakuraba, K. Izumi, T. Iwase, S. Bosu, K. Saito, K. Takanashi, Y. Miura, K. Futatsukawa, K. Abe, M. Shirai, Mechanism of large magnetoresistance in Co 2 MnSi/Ag/Co 2 MnSi devices with current perpendicular to the plane, Phys. Rev. B 82 (2010) 094444.

[27] R. Fetzer, J.-P. Wüstenberg, T. Taira, T. Uemura, M. Yamamoto, M. Aeschlimann, M. Cinchetti, Structural, chemical, and electronic properties of the Co 2 MnSi (001)/MgO interface, Phys. Rev. B 87 (2013) 184418.

[28] J. Chen, Y. Sakuraba, K. Yakushiji, Y. Kurashima, N. Watanabe, J. Liu, S. Li, A. Fukushima, H. Takagi, K. Kikuchi, S. Yuasa, K. Hono, Fully epitaxial giant magnetoresistive devices with half-metallic Heusler alloy fabricated on polycrystalline electrode using three-dimensional integration technology, Acta Mater. 200 (2020) 1038–1045.

[29] B. Wu, H. Yuan, A. Kuang, Y. Feng, H. Chen, Tunable magnetism and half-metallicity in bulk and (1 0 0) surface of quaternary Co2MnGe1− xGax Heusler alloy, J. Phys. D: Appl. Phys. 44 (2011) 405301.

[30] S. Konoplyuk, L. Kozlova, V. Kokorin, A. Perekos, O. Kolomiets, Magnetic states in ensemble of ferromagnetic nanoparticles in Cu-Mn-Al alloy, Nanoscale Res. Lett. 11 (2016) 1–5.

[31] C.A. Canbay, Z.K. Genc, M. Sekerci, Thermal and structural characterization of Cu–Al–Mn–X (Ti, Ni) shape memory alloys, Appl. Phys. A 115 (2014) 371–377.

[32] S. Yang, F. Zhang, J. Wu, Y. Lu, Z. Shi, C. Wang, X. Liu, Superelasticity and shape memory effect in Cu–Al–Mn–V shape memory alloys, Mater. Des. 115 (2017) 17–25.

[33] D. Singh, R. Tiwari, O. Srivastava, Structural and magnetic properties of Cu50Mn25Al25− xGax Heusler alloys, J. Magn. Magn. Mater. 328 (2013) 72–79.

[34] J. Kunzler, T. Grandi, W. Schreiner, P. Pureur, D. Brandão, Spin-disorder resistivity in the Cu2Mn (Al1− xSnx) heusler alloys, J. Phys. Chem. Solids 41 (1980) 1023–1026.

[35] G.F. Dong, L.P. Gai, X.L. Zhang, Phase transformation, thermoelastic and magnetic properties of Ni50Mn30Ga20−xCux ferromagnetic shape memory alloys, Mater. Sci. Eng.: B 178 (2013) 857–862.

[36] A. Wójcik, W. Maziarz, M.J. Szczerba, M. Sikora, J. Dutkiewicz, E. Cesari, Tuning magneto-structural properties of Ni44Co6Mn39Sn11 Heusler alloy ribbons by Fe-doping, Mater. Sci. Eng.: B 209 (2016) 23–29.

[37] N.V. Nong, L.T. Tai, N.T. Huy, N.T. Trung, C.R.H. Bahl, R. Venkatesh, F.W. Poulsen, N. Pryds, Structural, magnetic and magnetocaloric properties of Heusler alloys Ni50Mn38Sb12 with boron addition, Mater. Sci. Eng.: B 176 (2011) 1322–1325.

[38] S. Mishra, T. Yadav, R. Yadav, A.B. Puthirath, L. Deng, M. Adnani, C.-W. Chu, R. Vajtai, P. Ajayan, K. Biswas, Effect of Ga substitution on structural and magnetic properties of Fe50Mn25Al25-xGax Heusler alloys, J. Alloy. Compd. (2020) 156756.

[39] T. Block, M. Carey, B. Gurney, O. Jepsen, Band-structure calculations of the half-metallic ferromagnetism and structural stability of full-and half-Heusler phases, Phys. Rev. B 70 (2004) 205114.

[40] H. Ishikawa, R.Y. Umetsu, K. Kobayashi, A. Fujita, R. Kainuma, K. Ishida, Atomic ordering and magnetic properties in Ni2Mn(GaxAl1−x) Heusler alloys, Acta Mater. 56 (2008) 4789–4797.

[41] M. Bohra, M. de Weerd, V. Fournee, R. Mandal, N. Mukhopadhyay, R. Chatterjee, G. Sastry, Structural, tribological and resistivity studies of Ga substituted (Al71− xGax) Pd21Mn8 icosahedral and other intermetallic phases, J. Alloy. Compd. 551 (2013) 274–278.

[42] J.-M. Dubois, New prospects from potential applications of quasicrystalline materials, Mater. Sci. Eng.: A 294 (2000) 4–9.

[43] S. Kang, J. Dubois, J. Von Stebut, Tribological properties of quasicrystalline coatings, J. Mater. Res. 8 (1993) 2471–2481.

[44] L.Q. Jiang, J.K. Guo, H.B. Liu, M. Zhu, X. Zhou, P. Wu, C.H. Li, Prediction of lattice constant in cubic perovskites, J. Phys. Chem. Solids 67 (2006) 1531–1536.

[45] H. Zhang, W. Liu, X. Dai, X. Zhang, H. Liu, X. Yu, G. Liu, Synthesis, structure, magnetic and half-metallic properties of Co2− xRuxMnSi (x= 0, 0.25, 0.5, 0.75, 1) compounds, IUCrJ 7 (2020) 113–120.

[46] Y. Zhang, X. Xu, Predicting doped MgB2 superconductor critical temperature from lattice parameters using Gaussian process regression, Phys. C: Supercond. Appl. 573 (2020) 1353633.

[47] Y. Zhang, X. Xu, Yttrium barium copper oxide superconducting transition temperature modeling through Gaussian process regression, Comput. Mater. Sci. 179 (2020) 109583.

[48] Y.C. Yabansu, A. Iskakov, A. Kapustina, S. Rajagopalan, S.R. Kalidindi, Application of Gaussian process regression models for capturing the evolution of microstructure statistics in aging of nickel-based superalloys, Acta Mater. 178 (2019) 45–58.

[49] Q. Liu, H. Wu, M.J. Paul, P. He, Z. Peng, B. Gludovatz, J.J. Kruzic, C.H. Wang, X. Li, Machine-learning assisted laser powder bed fusion process optimization for AlSi10Mg: New microstructure description indices and fracture mechanisms, Acta Mater. 201 (2020) 316–328.

[50] Z. Guo, L. Pan, H. Qiu, X. Zheng, Z. Liu, Structural and magnetic phase transition in quinary Ni45Co5 (Mn, In, Sn) 50 Heusler alloy, J. Alloy. Compd. 615 (2014) 316–321.

[51] T. Yadav, D. Singh, R.R. Shahi, M. Shaz, R. Tiwari, O. Srivastava, Formation of quasicrystalline phase in Al70− x Ga x Pd17Mn13 alloys, Philos. Mag. 91 (2011) 2474–2481.

[52] P. Joy, S. Date, Comparison of the zero-field-cooled magnetization behavior of some ferromagnetic and ferrimagnetic systems, J. Magn. Magn. Mater. 218 (2000) 229–237.

[53] M. Zhang, G. Liu, Y. Cui, H. Hu, Z. Liu, J. Chen, G. Wu, Y. Sui, Z. Qian, X. Zhang, Magnetism and transport properties of melt-spun ribbon Cu2MnAl Heusler alloy, J. Magn. Magn. Mater. 278 (2004) 328–333.

[54] P. Mohn, E. Supanetz, Spin ordering in Fe3-x Mn x Si Heusler alloys, Philos. Mag. B 78 (1998) 629–636.

[55] M.M. Mallick, S. Vitta, Enhanced magnetic moment and curie temperature due to co-substitution in Heusler alloys Fe 2− x Co x MnSi, J. Mater. Sci.: Mater. Electron. 29 (2018) 1420–1425.

[56] J. Robinson, P. McCormick, R. Street, Structure and properties of Cu2MnAl synthesized by mechanical alloying, J. Phys.: Condens. Matter 7 (1995) 4259.

[57] J. Tobola, J. Pierre, S. Kaprzyk, R. Skolozdra, M. Kouacou, Electronic structure and magnetism in Co-Ni Heusler compounds, J. Magn. Magn. Mater. 159 (1996) 192–200.
[58] S. Thota, J. Kumar, Sol–gel synthesis and anomalous magnetic behaviour of NiO nanoparticles, J. Phys. Chem. Solids 68 (2007) 1951–1964.
[59] W. Duan, S. Lu, Z. Wu, Y. Wang, Size effects on properties of NiO nanoparticles grown in alkalisalts, J. Phys. Chem. C 116 (2012) 26043–26051.
[60] Z.-Y. Chen, Y. Chen, Q. Zhang, X. Tang, D. Wang, Z. Chen, P. Mascher, S. Wang, Vacancy-induced ferromagnetic behavior in antiferromagnetic NiO nanoparticles: a positron annihilation study, ECS J. Solid State Sci. Technol. 6 (2017) P798.
[61] B. Banerjee, On a generalised approach to first and second order magnetic transitions, Phys. Lett. 12 (1964) 16–17.
[62] C. Climent, S. Vela, J. Jornet-Somoza, M. Deumal, Revising the common understanding of metamagnetism in the molecule-based bisdithiazolyl BDTMe compound, Phys. Chem. Chem. Phys. 21 (2019) 12184–12191.
[63] M.G. Brik, I.V. Kityk, Modeling of lattice constant and their relations with ionic radii and electronegativity of constituting ions of A2XY6 cubic crystals (A=K, Cs, Rb, Tl; X=tetravalent cation, Y=F, Cl, Br, I), J. Phys. Chem. Solids 72 (2011) 1256–1260.
[64] H.B. Luo, C.M. Li, Q.M. Hu, R. Yang, B. Johansson, L. Vitos, Theoretical investigation of the effects of composition and atomic disordering on the properties of Ni2Mn(Al1−xGax) alloy, Acta Mater. 59 (2011) 971–980.
[65] Y. Zhang, X. Xu, Machine learning lattice constants for cubic perovskite A22+BB′O6 compounds, CrystEngComm 22 (2020) 6385–6397.